TRANSIENT MODELING OF HOST ROCK FOR A DEEP BOREHOLE NUCLEAR WASTE REPOSITORY

by
Nazar Lubchenko

B.S. Applied Physics and Mathematics
Moscow Institute of Physics and Technology, 2010
M.S. Applied Physics and Mathematics
Moscow Institute of Physics and Technology, 2012

SUBMITTED TO THE DEPARTMENT OF NUCLEAR SCIENCE AND ENGINEERING
IN PARTIAL FULFILLMENT OF THE REQUIREMENTS FOR THE DEGREE OF

MASTER OF SCIENCE IN NUCLEAR SCIENCE AND ENGINEERING
AT THE
MASSACHUSETTS INSTITUTE OF TECHNOLOGY
JUNE 2015

Signature of Author: Signature redacted
Department of Nuclear Science and Engineering
May 19, 2015

Certified by: Signature redacted
Emilio Baglietto
Assistant Professor of Nuclear Science and Engineering
Thesis Supervisor

Certified by: Signature redacted
Jacopo Buongiorno
Associate Professor of Nuclear Science and Engineering
Thesis Reader

Certified by: Signature redacted
Michael J. Driscoll
Professor Emeritus of Nuclear Science and Engineering
Thesis Reader

Accepted by: Signature redacted
Mujid S. Kazimi
TEPCO Professor of Nuclear Engineering
Chair, Department Committee on Graduate Students

Transient Modeling of Host Rock for a Deep Borehole Nuclear Waste Repository

by
Nazar Lubchenko

Submitted to the Department of Nuclear Science and Engineering
on May 19, 2015 in Partial Fulfillment of the Requirements for the Degree of
Master of Science in Nuclear Science and Engineering

Abstract

This work describes a framework built to simulate the thermal and hydrological processes in a deep borehole repository of spent nuclear fuel. Such simulation requires a fully coupled solver, capable of capturing the processes at the scale of tens of kilometers and millions of years.

The MOOSE framework was chosen for this purpose, where the FALCON application, developed at INL, was adopted as baseline. This application had previously been applied for simulation of fluid flow and heat transport in geothermal reservoirs, and therefore provided a valuable reference.

Additional features were implemented in FALCON in order to simulate deep borehole repositories. Solver options were adjusted for best performance. Code verification was performed on Rayleigh-Bénard convection in a porous medium. Cross-code validation was performed between the FALCON code and the FEHM code on a single borehole test case, and the thermal results were further compared to analytical and simplified numerical models, confirming the potential existence of a second peak of temperature at the scale of thousands of years.

Two configurations for the borehole repository were analyzed. The first one consisted of an infinite array of boreholes, which allows one to significantly simplify the geometry, boundary conditions, and test code features. A parametric study of input parameters such as rock permeability, borehole spacing, and pitch length, was performed to assess thermal behavior of the repository. Analysis of the results led to the conclusion that the water flow in the caprock is driven mostly by thermal expansion of water. The displacement length of the water front was found to be negligible in comparison to the depth of the repository.

The second configuration included a semi-infinite array of boreholes. This representation is a more realistic approximation of an actual repository, since it includes the modeling of the undisturbed rock surrounding the emplacement zone. It was shown that in this configuration convection can originate between the emplacement region and the rock outside the repository. At rock permeability higher than 10^{-16} m^2 this mechanism can lead to an escape length of the water front larger than the burial depth. However, it was shown that the salinity gradient in the underground water can suppress convection and effectively eliminate water escape.

Thesis Supervisor: Emilio Baglietto
Title: Assistant Professor of Nuclear Science and Engineering

Acknowledgements

First and foremost, I would like to thank my thesis advisor, Prof. Emilio Baglietto. I would not have been able to complete this work without his encouragement and advice. In fact, I would not have even started this work, because Prof. Baglietto was the one who offered this project to me almost three years ago. I am also thankful to him for his infinite patience and support. Many thanks also go to Prof. Michael Driscoll for his kind guidance in the tough process of thesis writing, and invaluable lessons of human wisdom and English grammar. A very special "Thank you!" goes to Prof. Jacopo Buongiorno, the reader of this thesis, for wise and timely comments on my work.

Like many other projects done at MIT, this thesis would not have been possible without the cooperation with scientists from outside of MIT. I am talking about the INL researcher Robert Podgorney, who wrote FALCON, and the SNL researcher Bill Arnold, who provided the input data and the results for the cross-code validation.

This project was funded by the United States Department of Energy Nuclear Engineering University Program (NEUP) grant "Optimization of Deep Borehole Systems for HLW Disposal," which is gratefully acknowledged.

I would like to thank all the people who helped me in my struggle with the MOOSE framework: MOOSE developer Derek Gaston, Eugeny Sosnovsky, Prof. Michael Short, and the entire community of MOOSE users worldwide.

I would like to acknowledge here my colleagues from MIT. Special thanks to Ethan Bates who helped me to get familiar with the project, and provided a lot of very useful information and references on the topic, which was originally completely unknown for me. Additionally, I would like to thank the whole CFD team of Prof. Baglietto for the invaluable discussion and critique of the results at the group meetings. Also, I would like to wish good luck to Mariana Rodriguez Buño, who will continue developing this work.

I would also like to thank my friends for their support during my studies at MIT. Special thanks go to Nadia Shifrin for moral support and patience, and to my parents Taras and Olga Lubchenko.

Finally, I should acknowledge the importance of the events in my home country in the past year. These events did not always encourage me, but they were very important to me during my graduate studies at MIT.

Table of Contents

List of Figures

List of Tables

Nomenclature

Latin Symbols

Symbol	Meaning	Units
A	Cross-section area	m^2
c	Specific heat capacity	J/(kg·K)
C	Scaling coefficient	-
D	Diffusion coefficient	m^2/s
d	Particle diameter	m
E	Energy	J
g	Acceleration due to gravity	m/s^2
H	Height	m
J	Dissolved species flux	$kg/(m^2 \cdot s)$
j	Superficial (Darcy) velocity	m/s
K	Permeability	m^2
k	Thermal conductivity	W/(m·K)
L	Length	m
n	Normal vector to the boundary	-
N	Number of atoms	-
Q	Volumetric flux	m^3/s
q	Power	W
q''	Heat flux	W/m^2
q'''	Volumetric heat source	W/m^3
P	Pitch length (boreholes spacing)	m
P	Pressure	Pa
Pe	Péclet number	-
R	Residual	-
r	Radius	m
Ra	Rayleigh number	-
Re	Reynolds number	-
T	Temperature	K
t	Time	s
u	Variable in a weak form derivation	-
V	Volume	m^3
v	Average linear velocity	m/s
z	Depth	m

Greek Symbols

Symbol	Meaning	Units
α	Dispersion coefficient	m
β_P	Compressibility	Pa^{-1}
β_T	Thermal expansion coefficient	K^{-1}
ε	Porosity	-
λ	Decay constant	s^{-1}
μ	Viscosity	Pa·s
ρ	Density	kg/m^3
τ	Tortuosity	-
φ	Trial functions in weak forms of equations	-
ψ	Test functions in weak forms of equations	-
Ω	Domain of a single finite element	-

Subscripts

Subscript	Meaning
b	brine
c	cooling
cr	critical
eff	effective
f	fluid
P	pressure
p	porous
r	rock
S	solute
s	seal
T	temperature
w	water

Acronyms

Acronym	Meaning
CFL	Courant-Friedrichs-Lewy number
CL	CenterLine
FALCON	Fracturing And Liquid CONvection
FEHM	Finite Element Heat and Mass transfer code
HLW	High-Level Waste
JFNK	Jacobian-Free Newton Krylov method
MOOSE	Multiphysics Object Oriented Simulation Environment
PJFNK	Preconditioned Jacobian-Free Newton Krylov method

PWR	Pressurized Water Reactor
SKB	Swedish Nuclear Fuel and Waste Management Company
SNF	Spent Nuclear Fuel
SNL	Sandia National Laboratories
tHM	metric tons of Heavy Metal

1. Introduction

1.1. Motivation

After the suspension of work on the Yucca Mountain nuclear waste repository, currently no approved concept for used nuclear fuel disposal exists in the United States [1]. The total amount of high-level waste accumulated after more than 50 years of commercial usage of nuclear reactors is estimated at around 69,000 tHM [2].

In 1983 deep boreholes were suggested as a viable solution to this problem [3]. The concept includes drilling a number of boreholes up to 5 km deep into a granitic region of the Earth's crust. Canisters with spent nuclear fuel are placed in the bottom few kilometers of the borehole, which is later sealed with concrete, bentonite or cement. Compared to shallow repositories, canisters with spent nuclear fuel are placed significantly deeper into the boreholes, further away from ground surface and aquifers. Low-permeability rock creates a natural barrier that prevents radionuclides from spreading. Deep granite rock is typically a chemically reducing environment, which reduces the solubility of most radionuclides and transuranics. All the above characteristics lead to an augmented isolation of the radioactive materials from the biosphere. In addition, solid granite formations are very common in the US and the rest of the world. Currently deep borehole waste disposal is the only significantly investigated alternative to shallow repositories.

Since the concept of deep boreholes for spent nuclear fuel was proposed a number of studies were performed to assess its reliability. They range from analytical derivations [4] to 2D simulations [5] of heat transfer behavior. A number of studies were performed in Sweden at SKB. They include analytic derivation of groundwater flow rate around single boreholes represented by an instantaneous point source [6]. Later this approach was extended to linear heat sources, complex decay heat with several components, and effect of salinity on the water flow [7]. A three-dimensional numerical study of arrays of deep boreholes was performed at Sandia National Laboratories. A finite volume code FEHM [8] was used to study coupled fluid flow, heat transfer, and mechanical properties of the rock [9]. However, the code did not geometrically resolve the boreholes, which were instead replaced by a homogenized large element.

1.2. Objectives

For a rigorous justification of the boreholes concept a fully coupled 3D code is essential. The objective of this project was to develop a modeling capability that includes thermal, hydrologic and chemical transport, and can be extended in the future by including modeling of the mechanical properties of the rock. The code should be capable of resolving processes on different length scales, which vary from tens of centimeters (borehole diameter) to tens of kilometers (site size). The code should be capable of running on time scales from years in the beginning of simulation to the total time of 1 million years, which is the regulated time period of confinement.

To reach the goal, the FALCON application [10], developed in the MOOSE framework [11], was selected as starting point. The goal of this work was to implement thermal and fluid models to existing applications, implement in the application all necessary models and correlations and optimize the code for deep boreholes modeling. The work focused mostly on development and demonstration of a tool that could be used for realistic geometries and conditions. For this reason, rather than analyzing site specific properties of water, rock, canister, and seal, it was shown that a

wide range of input parameters can be analyzed in this application by running approximations of real correlations with specified tolerances.

A further objective of the work has been to leverage the tool to identify potential failure mechanisms and radionuclide transport paths. The provided findings may be used to improve the design of the borehole repository, including optimal pitch length and number of boreholes, maximum depth of the repository, emplacement length, and canister properties like diameter and filling material. The results could be used to support the site selection, and afterward an extension of this MOOSE-based analysis could be adopted to support the site license application.

1.3. Selection of Computational Framework

The discussed requirements on the computational capabilities impose restrictions to the numerical methods being used. Conventional finite volume codes, for example, while offering advantages in memory usage and model implementation, cannot perform equally well with time steps varying by a factor of 1,000,000 and on cells with aspect ratio of the order of 1,000. A possible approach to overcome this limitation is to use very fine mesh and very small time steps. However, this would make the solution impracticable due to the computational cost.

Another approach is to use a finite element solution method. Finite element codes can handle elongated elements inside the borehole, which allows resolving the borehole diameter while keeping the number of layers in the vertical direction relatively small. Additionally, finite element codes offer an excellent base for coupling of all physical phenomena, thus allowing the use of relatively large time steps.

The MOOSE (Multiphysics Object Oriented Simulation Environment) framework was chosen in this work, as it satisfies all the discussed requirements. It is a C++ framework designed at Idaho National Laboratory for solving strongly coupled multi-physics problems using a robust finite elements solver [11, 12]. The framework is built on top of the adaptive finite element library libMesh and allows easy implementation of different physical processes as separate kernels. Each kernel is an object that represents the residual of the solution due to one physical phenomenon. A number of applications have been developed using MOOSE in the past. One of them is FALCON (Fracturing And Liquid CONvection). This application was developed at Idaho National Laboratories to model multiphase fluid flow, heat transport, and rock deformation for geothermal reservoirs [10]. This application already included heat transport in the rock and a two-phase formulation of fluid mechanics and was used in this project.

2. Background

2.1. Deep Boreholes Concept Overview

The concept of deep boreholes was suggested in 1983 [3] and, along with seabed disposal, became one of two options recommended by the Department of Energy (DOE). The main idea is to dispose of canisters with high-level waste (HLW) and spent fuel in very deep (up to 5 km) boreholes. Typically a diameter around 34 cm is assumed, which allows disposal of one assembly of a PWR in one 5-m-long canister. Drilling such boreholes is a routine operation for the oil and gas industry, so the total cost of the technology should be lower compared to other approaches.

The canisters with the fuel can be lowered to the bottom 2-3 km of the borehole, and sealed with low-permeable material like concrete, bentonite, or cement. After this the borehole should remain intact for the next one million years. Even if canisters degrade after emplacement, the layer of granite above should prevent radionuclides from escape to the environment.

Compared to the now-abandoned Yucca Mountain repository project, deep boreholes rely more intensely on geologic properties. There are some geological observations which justify the above assumption. The first example of a geologic repository is the natural nuclear reactor in Oklo [13]. It is believed that 1.7 billion years ago a natural chain reaction occurred in rich uranium ore deposits. The isotope composition of neodymium and ruthenium found on site was different from the naturally occurring isotope composition. This leads to the conclusion that all decay products stayed with the original uranium ore for billions of years without migrating to the surface.

Another example is radioactive dating of the groundwater. Different methods involving various isotopes (H^3, C^{14}, I^{129}, and Cl^{36}) have been used to determine the age of the water samples from different depths in granitic rocks [14]. The presence of tritium ($t_{1/2}$ = 12.3 y) indicates that the surface layer actively communicates with the atmosphere and is not more than about 60 years old. In granitic rocks tritium is typically found down to 200 m. C^{14} ($t_{1/2}$ = 5,730 y) can be found in deeper regions. For even deeper regions longer-living isotopes of Cl^{36} ($t_{1/2}$ = 301,000 y) and I^{129} ($t_{1/2}$ = 15 My) are used [14, 15]. A general conclusion is that the residence time of water below 1000 m exceeds the time required for most of the radionuclides to decay.

Therefore, the environment of the deep boreholes prevents radionuclide escape from the deep borehole. For this reason, there is no need to build additional engineered barriers, except for the seal or plug, as explained below. However, borehole drilling induces perturbations to the existing system. Borehole drilling can cause stresses in the granite which can cause formation of cracks. The borehole's seal consists of material different from the surrounding granite, which potentially can create a gap between the seal and the borehole wall. The high decay heat of canisters causes thermal expansion of the adjacent rock, which can induce wall failure and increase granite permeability around the borehole. In addition, decay heat causes water expansion and induces water flow.

2.2. Governing Equations

2.2.1. Thermal Model

It is typical to assume the rock and fluid in the pores are in local thermal equilibrium. This assumption is justified by the fact that pores have sizes of the order of micro- and millimeters, and

the fluid flow is extremely low. With this assumption, consider the heat transport equation in the most general form:

$$(\rho c)_{eff}\frac{\partial T}{\partial t} = \nabla\cdot(k_{eff}\nabla T) + q''' - \rho_f c_f \vec{j}\cdot\nabla T, \tag{2.1}$$

$$(\rho c)_{eff} = \varepsilon\rho_f c_f + (1-\varepsilon)\rho_r c_r, \tag{2.2}$$

$$k_{eff} = \varepsilon k_f + (1-\varepsilon)k_r. \tag{2.3}$$

Here, the following nomenclature is used:

ρ	density of the material, kg/m^3
c	specific heat capacity of the material, J/(kg·K)
T	temperature, K
t	time, s
k	thermal conductivity, W/(m·K)
q'''	volumetric heat generation (due to radioactive decay in the fuel or in the host rock), W/m^3
$\vec{j}$	superficial velocity, which will be defined in Section 2.2.2, m/s

Indices *eff* denote effective values, *f* denote fluid properties, and *r* denote rock properties.

If the geothermal flux q'' is very high or the rock properties vary significantly then Eq. (2.1) may have multiple unsteady solutions, including ones with convection of ground water. Such regions are undesirable for a deep borehole repository and fuel emplacement. In the absence of any factors that break the equilibrium the system reaches steady state with uniform heat flux through the lithosphere. If the temperature across any horizontal plane is uniform then the water flow should become zero, and the equation (2.1) turns into

$$\frac{\partial}{\partial z}\left(k_{eff}\frac{\partial T}{\partial z}\right) + q''' = 0. \tag{2.4}$$

Usually the heat generation in granite is low and its contribution to the geothermal flux is negligible compared to the heat flux on the bottom of the modeled region q''. In this case Eq. (2.4) can be solved analytically for temperature as a function of depth only:

$$T(z) = T(0) + \int_z^0 \frac{q''}{k_{eff}(z,T)}dz. \tag{2.5}$$

If the thermal conductivity k_{eff} is constant then (it should be noted that z is negative):

$$T(z) = T(0) + \frac{q''}{k_{eff}}z. \tag{2.6}$$

This solution is used as an initial condition for the transient analysis of the deep borehole repository performance. The initial temperature of the canisters was assumed to be the same as that of the surrounding rock. The real canister's temperature may be higher or lower than that of the rock, however, heat added or removed from the system is negligible compared to the total heat produced by the canisters in the long term, so this assumption does not affect the final results.

After the canisters emplacement the temperature distribution changes significantly. Each fission product and actinide decays according to the first-order differential equation:

$$\frac{dN}{dt} = -\lambda N, \tag{2.7}$$

where N is the number of atoms of the corresponding radionuclide, and λ is the decay constant. The solution to eq. (2.7) is the well-known exponential law:

$$N = N_0 e^{-\lambda t}. \tag{2.8}$$

If each decay produces energy E, then the total power generated by the sample also follows the exponential law:

$$q''' = \frac{\lambda E N_0 e^{-\lambda t}}{V} = q'''_0 e^{-\lambda t}. \tag{2.9}$$

For the mixture of the elements this dependence becomes more complex. At first, the overall heat generation consists of heat generation by all the elements that undergo decay, with different decay constants. But some elements form decay chains, in which the daughter radionuclides are produced from parent radionuclides and decay later. Heat generation by these elements does not follow the simple exponential decay (2.9). Nevertheless, the total heat generation can be obtained numerically for any initial composition of the spent fuel. The tables for the decay heat of the commercial spent fuel from different types of reactors are widely available [16, 17].

Typically canisters cannot be resolved in geological simulations, since each canister contains hundreds of fuel rods with non-uniform burnup, and hence, decay power. For this reason all canisters are replaced with a homogenized material. The heat generation in the model is spread uniformly inside the canister. The canisters are replaced with a material with effective density, heat capacity, and thermal conductivity. The density is averaged to conserve the total mass of the canister, and the specific heat capacity is averaged to conserve total heat capacity. The effective heat conductivity is adjusted so that the peak temperature in the homogenized canister corresponds to the peak temperature in the spent fuel rods. The details of the homogenization process were described by C. Hoag [18].

Equation (2.1) was used for transient thermal analysis. This is an advection-diffusion equation with thermal diffusivity

$$D_T = \frac{k_{eff}}{(\rho c)_{eff}}, \tag{2.10}$$

which has the order of 10^{-6} m^2/s. The surface boundary condition was set to a constant temperature of 10 °C, which represents a typical average surface temperature for the north temperate zone. Underground axial boundary conditions for shallow repositories were discussed in [4]. The general recommendation was to set the axial boundary as far as possible, with distance of 10 times the depth of the repository, sufficient to have no effect on the solution around the repository. Such an approach is impossible for deep boreholes, since it would require the domain size of 50 km. Another approach was used in the FEHM code [9], when the boundary was set at 7 km with a constant heat flux condition.

From the analysis of the isotropic heat diffusion equation one can derive the characteristic length of heat diffusion

$$L = \sqrt{D_T t}. \tag{2.11}$$

Since the total simulation time is 1 million years the characteristic length at this moment is $L \approx 5$ km. Preliminary runs of the code were made with a thermal boundary at 10 km with constant heat flux and constant temperature conditions and they show no effect of the boundary type. For this reason the axial boundary was set at 10 km with fixed heat flux.

Lateral boundary conditions depend on the type of geometry considered. For the geometries with symmetry planes the boundary was set as a symmetry boundary with zero heat flux through it. The outer boundary in the open geometries was set as no-flux, far enough so that it does not interfere with the solution. In all cases the temperature was not a limiting variable for the lateral boundary distance.

2.2.2. Fluid Model

Several important assumptions should be made to derive the governing equations of water flow. It is assumed that the phenomena occurring at the ground surface and in the aquifer do not affect the behavior of water deep underground. For this reason, the water table is assumed to be at the top of the computational domain. The favorable locations for the deep borehole repository have low geothermal fluxes and temperature gradients. For this reason the pressure is always high enough for water to be liquid at any moment of time and in any location. The buildup of gases in the borehole is also neglected. With these assumptions only single phase fluid is considered and the capillary effects can be neglected.

The underground water can be confined in isolated and connected pores. The number of isolated pores increases with depth. The pressure in such pores deviates from hydrostatic and is more close to the lithostatic (overburden) pressure [14, p. 167]. However, isolated pores do not contribute to water flow. The water in connected pores is at hydrostatic pressure. Assuming isotropic properties of the rock consider the general form of Darcy's law:

$$\nabla P - \rho_f \vec{g} + \frac{\mu}{K} \vec{j} = 0. \tag{2.12}$$

Here, the following nomenclature was used:

P	pressure, Pa
$\vec{g}$	acceleration due to gravity, m/s^2
μ	water viscosity, Pa·s
K	host rock permeability, m^2
$\vec{j}$	superficial (Darcy) velocity, m/s

It should be noted that $\vec{j}$ is the superficial velocity defined as

$$j = \frac{Q}{A}, \tag{2.13}$$

where Q is a volumetric flow rate, m^3/s, and A is a cross-section area, m^2. The superficial velocity is related to the average linear velocity or seepage velocity $\vec{v}$ of the flow in pores:

$$\vec{j} = \varepsilon \vec{v}, \tag{2.14}$$

where ε is the effective porosity of the rock.

Equation (2.12) is valid for slow flows. Typically it is assumed that velocity is proportional to the pressure gradient if

$$\mathrm{Re}_{cr} = \frac{\rho_f j d_p}{\mu} < 10 \tag{2.15}$$

where d_p is the flow length scale. In many applications particle diameter is taken as the length scale. For the flows in low-porosity media it is difficult to determine particle or fracture diameters and it is suggested that $d_p = \sqrt{K}$ or $d_p = \sqrt{K/\varepsilon}$ [19]. In any case Re_{cr} does not exceed 10^{-8}, so Eq. (2.12) can be certainly applied.

Before the fuel emplacement the distribution of the pressure with depth is hydrostatic, and can be obtained from Eq. (2.12):

$$P(z) = P(0) + \int_z^0 \rho_f(T,P) g \, dz. \tag{2.16}$$

Equation (2.16) specifies the initial water pressure in the system. It should be noted that it does not depend on porosity or permeability of the rock.

After fuel emplacement water starts to move due to expansion and pressure gradients. Assuming that the flow is always saturated, it follows the continuity equation:

$$\frac{\partial(\varepsilon\rho_f)}{\partial t} + \nabla \cdot (\rho_f \vec{j}) = 0. \tag{2.17}$$

Combining Eqs. (2.12) and (2.17) one can get

$$\frac{\partial(\varepsilon\rho_f)}{\partial t} + \nabla \cdot \left(\frac{K\rho_f^{\,2}}{\mu} \vec{g} \right) - \nabla \cdot \left(\frac{K\rho_f}{\mu} \nabla P \right) = 0. \tag{2.18}$$

As a first approximation rock porosity can be assumed constant. Then from the definition of water compressibility one has

$$\varepsilon \beta_{P,f} \rho_f \frac{\partial P}{\partial t} = \nabla \cdot \left(\frac{K\rho_f}{\mu} \nabla P \right) - \nabla \cdot \left(\frac{K\rho_f^{\,2}}{\mu} \vec{g} \right), \tag{2.19}$$

which is a diffusion equation of pressure. The characteristic diffusivity of pressure for this equation is

$$D_P = \frac{K}{\mu \varepsilon \beta_{P,f}}, \tag{2.20}$$

and for a typical deep borehole repository D_P has order of magnitude of 0.1 m^2/s.

Correct account of rock compressibility adds one more term to the final equation. The pressure in most of the rock is lithostatic, which is very different from the hydrostatic pressure. A very small fraction of rock near the fractures is affected by water pressure increase, so effective compressibility is lower than compressibility of the pure material of the rock (see p. 77 in [14]). Define a confined uniaxial compressibility of rock:

$$\beta_{P,r} = -\frac{\partial \varepsilon}{\partial P}. \tag{2.21}$$

Then the left side of Eq. (2.19) becomes [19]

$$\frac{\partial(\varepsilon\rho_f)}{\partial t} = \varepsilon\frac{\partial\rho_f}{\partial P}\frac{\partial P}{\partial t} + \rho_f\frac{\partial\varepsilon}{\partial P}\frac{\partial P}{\partial t} = \rho_f\frac{\partial P}{\partial t}\left(\varepsilon\beta_{P,f} + \beta_{P,r}\right), \tag{2.22}$$

and the whole equation turns into

$$\left(\varepsilon\beta_{P,f} + \beta_{P,r}\right)\rho_f\frac{\partial P}{\partial t} = \nabla\cdot\left(\frac{K\rho_f}{\mu}\nabla P\right) - \nabla\cdot\left(\frac{K\rho_f^{\,2}}{\mu}\vec{g}\right). \tag{2.23}$$

The characteristic diffusivity of pressure for this equation is [20]

$$D_P = \frac{K}{\mu\left(\varepsilon\beta_{P,f} + \beta_{P,r}\right)}, \tag{2.24}$$

Equations (2.19) or (2.23) were used for transient analysis of water flow. The top boundary was set as a fixed pressure boundary. This allows free exchange of water with the surroundings at the surface. Currently there is no model for the water exchange with aquifers. Such models can be implemented in future to correctly treat effects of dilution.

The lateral boundaries were set to impermeable on the symmetry planes:

$$\vec{j}\cdot\vec{n} = 0. \tag{2.25}$$

The outer boundary in open geometries was set at 20-40 km away to reduce the effect of the boundary on the solution.

The bottom boundary condition was set to impermeable boundary with zero flux through it. This represents the physical conditions at the great depth. Typically rock permeability and effective porosity decrease with depth. However, at the depth of 12-15 km a brittle-ductile transition in rock occurs due to high pressure and temperature. It is assumed that below the brittle-ductile transition pores at hydrostatic pressure tend to collapse so that porosity of connected pores goes to zero [14]. This means that at a certain point water flow instantly goes to zero. In the present work the boundary was set at 10 km; however, in the future it can be set at the depth of brittle-ductile transition specific for the location being analyzed.

2.2.3. Solute Transport

The groundwater can transport dissolved species. Two main groups of solutes are of interest in the present work. One of them is the salinity of water, and another is the radionuclides released from the canisters to the groundwater. The transport of both follows the same equations, however, the two groups are different for the analysis. The water salinity can reach values of 400

g/L. This concentration is high enough to change the equation of state of water. In contrast to this, the amount of soluble radionuclides in canisters is small compared to the amount of water available for it.

In the presence of solute Eq. (2.19) should be modified. In this case the continuity equation (2.17) should be written for water only, while the hydrostatic pressure term in Darcy's law (Eq. (2.12)) should include brine density ρ_b. Taking this into account Eq. (2.19) becomes

$$\varepsilon\beta_{P,f}\rho_f\frac{\partial P}{\partial t}=\nabla\cdot\left(\frac{K\rho_f}{\mu}\nabla P\right)-\nabla\cdot\left(\frac{K\rho_f\rho_b}{\mu}\vec{g}\right). \tag{2.26}$$

Through brine density water transport is coupled to the solute transport. There are three main mechanisms of solute transport: advection, diffusion, and dispersion. Diffusion in the open water is governed by Fick's first law:

$$\vec{J}=-D_f\nabla S, \tag{2.27}$$

where $\vec{J}$ is the mass flux of the solute, and S is the salinity or concentration of the solute in kg/m^3 or g/L.

In a porous medium the diffusion coefficient should be modified. At any cross-section in the rock with area A only εA of it is available for water flow and diffusion of solute through it. Additionally, the effect of tortuosity of the channels plays a role. For these reasons the diffusion coefficient should be modified [14]:

$$D_p=\frac{\varepsilon}{\tau}D_f, \tag{2.28}$$

where τ is tortuosity. Fick's law can be combined with the mass-balance equation to obtain Fick's second law:

$$\varepsilon\frac{\partial S}{\partial t}=D_p\nabla^2 S. \tag{2.29}$$

Mechanical dispersion is another mechanism that contributes to the transport. Typically it is expressed as an additional term to the diffusion coefficient [19, 14]:

$$D=D_p+\alpha v, \tag{2.30}$$

where α is the dispersion coefficient and v is the seepage velocity (Eq. (2.14)). Typically it is assumed that the dispersion coefficient is proportional to the characteristic length of the cracks [19, 14]:

$$\alpha=1.8d_p. \tag{2.31}$$

In the present work the values of the characteristic length and seepage velocity are low so that dispersion can be neglected compared to diffusion.

Pure advective transport of the solute can be written as

$$\frac{\partial S}{\partial t} = -\vec{v} \cdot \nabla S. \tag{2.32}$$

Taking into account Eq. (2.14) two Eqs. (2.29) and (2.32) can be combined into

$$\varepsilon \frac{\partial S}{\partial t} = \left(\frac{\varepsilon D_f}{\tau} + \frac{\alpha j}{\varepsilon} \right) \nabla^2 S - \vec{j} \cdot \nabla S. \tag{2.33}$$

Equation (2.33) is the governing equation of the solute transport and was implemented in FALCON. In the present work only salinity (not radionuclides) transport was modeled with Eq. (2.33). The initial conditions were set from the measurements of salinity in natural reservoirs. Boundary conditions were set to impermeable bottom and symmetry boundaries, fixed salinity at the surface and outer boundaries.

2.3. Reference Model Parameters

The performance of the deep borehole repository depends on many properties of rock at the site and repository design. It should be noted that neither a place for a repository nor final design of the boreholes and canisters has been selected. However, a set of realistic parameters is needed for testing of the code to make sure that the code can correctly treat all phenomena existing in the repository. Most of the parameters were taken consistent with previous research conducted at MIT [1, 5, 21, 22] and SNL [9, 23] to facilitate comparison and analysis of the results.

2.3.1. Rock Properties

Heat properties of the rock are site-specific, but in general they can be measured in laboratory conditions. Some of them like thermal conductivity may also depend on temperature, and density depends on pressure. However, such variations are typically lower than the uncertainty due to uncertain rock composition. For the sake of simplicity all thermal properties of the rock were assumed to be constant in time and uniform throughout the domain. However, temperature and pressure-dependent properties can also be implemented in MOOSE. A detailed summary of crystalline basement rock can be found in [21, p. 44]. Suggested values are taken as reference parameters and are summarized in Table 1.

In many civil applications granite is considered impermeable, with permeability estimated below 10^{-18} m^2 [19, p. 68]. However, the flows around deep boreholes can have a significant effect on the time scales of millions of years, so even this low permeability should be taken into account. Permeability of the granite varies depending on the method of measurement. Laboratory measurements of small samples typically predict low permeability [24], while in-situ measurements predict much higher permeability, of the order of 10^{-16} m^2 [25]. This is likely to be caused by larger cracks, which typically are absent in small samples studied in the laboratory facilities. Permeability is also likely to depend on depth. However, very few correlations exist for this dependence. The most notable was derived in [25] and was used in the FEHM code:

$$\log K\,[\mathrm{m}^2] = -3.2 \log z\,[\mathrm{km}] - 14. \tag{2.34}$$

However, in most of the runs uniform permeability was used. Other parameters include effective porosity of the rock and confined rock compressibility, which were also taken consistent with previous MIT studies [5, 21].

Table 1. Summary of rock properties.

Parameter	Value
Density	2750 kg/m^3
Thermal conductivity	3.0 W/(m·K)
Specific heat	790 J/(kg·K)
Geothermal flux	45 mW/m^2
Geological temperature gradient	15 °C/km
Surface temperature	10 °C
Surface pressure	101,325 Pa
Permeability	10^{-16} m^2
Porosity	0.01
Confined compressibility of rock	4.62×10^{-12} Pa^{-1}
Solute diffusion in water	10^{-9} m^2/s

Various correlations for salinity of water with depth were developed in the past. Typically linear dependence of salinity with depth is derived in analytical studies [7] and is used in simulations [23]. However detailed study of data from different sources show that salinity reaches saturation at a depth around 2 km. A correlation developed at MIT for water salinity was used in the present work [22]:

$$\begin{aligned} &S\,[\mathrm{kg/m^3}] = 1.234\times10^{-4}\,z\,[\mathrm{m}]^2 + 0.059419z\,[\mathrm{m}] + 5.844, \quad z > -1930\,\mathrm{m} \\ &S = 350\,\mathrm{kg/m^3}, \quad z < -1930\,\mathrm{m} \end{aligned} \tag{2.35}$$

This correlation was modified to remove unphysical negative salinity in the uppermost region:

$$\begin{aligned} &S = 5.844\,\mathrm{kg/m^3}, \quad z > -480\,\mathrm{m} \\ &S\,[\mathrm{kg/m^3}] = 1.234\times10^{-4}\,z\,[\mathrm{m}]^2 + 0.059419z\,[\mathrm{m}] + 5.844, \quad -480\,\mathrm{m} > z > -1930\,\mathrm{m} \\ &S = 350\,\mathrm{kg/m^3}, \quad z < -1930\,\mathrm{m} \end{aligned} \tag{2.36}$$

No horizontal variation in initial salinity profile is usually assumed. This assumption is valid if the rock is located far from the sea or large saline lakes. However, due to water flow caused by expansion or convection horizontal variation around the deep borehole repository may appear after the fuel emplacement.

2.3.2. Repository Design

Different deep borehole repository designs were developed by various groups. This includes designs developed in SKB, Sweden [26], University of Sheffield [27], United Kingdom, SNL [28] and MIT [21, 29].

Typically the borehole is designed to accommodate fuel at the depth of 3 to 5 km; however, more shallow concepts with disposal zone between 1 km and 2 km have been proposed [29]. The diameter of the boreholes is usually limited by the drilling technologies available and size of the canisters used. Usually canisters are designed so that they can accommodate full fuel assemblies without their reprocessing [21]. The borehole diameter can be larger in the plug zone than in the emplacement zone; however, during the modeling this difference was usually neglected.

One borehole of this design can accommodate up to 400 5-m-long canisters with spent nuclear fuel. The total mass of spent fuel loading is 500 kgHM per canister, or 200 tHM per borehole. An array of 20×20 boreholes in a square lattice is assumed as a reference design for the repository that can satisfy the needs of the US. The borehole spacing is limited by many factors like thermal and hydrologic performance. In the past it was shown that very close spacing may cause significant increase in repository temperature after around 10,000 years since emplacement [5]. This limits the minimum distance between boreholes at 200 m.

Complete resolution of all features of the fuel canisters with the mesh is impossible. For this reason canisters containing the fuel are treated as a homogeneous medium. All thermal properties of the canisters like volumetric decay power, thermal conductivity, density, and specific heat capacity are assumed to be uniform. Properties like volumetric decay heat, density, and specific heat capacity are taken so that total values of power, mass, and heat capacity are conserved. The value of thermal conductivity is usually adjusted so that peak temperature in the homogenized geometry matches the peak temperature in the canister. The process of homogenization was studied in detail analytically by Hoag [18], and can be studied numerically on the scale of the canisters.

The heat generation of decay products of nuclear fuel is available as the ANS standard [17]. Heat generation of real canisters varies from assembly to assembly depending on the reactor type, burnup, and cooling time. Typically it is approximated with an average decay power with some level of conservatism. An overview of different correlations was made in [30]. For the sake of consistency with previous research two correlations for average decay power were used in the present study.

The first correlation was derived from [30], scaled to 57 MWh/kg burnup as a conservative assumption. This function was previously used at MIT [5, 21]:

$$q'''(t) = 2176\left(\frac{t_c}{t_c + t}\right)^{0.75} \text{ W/m}^3, \tag{2.37}$$

where $t_c = 25$ y is cooling time.

In the validation of the code with the FEHM code (Section 5.2) the table for characteristics of average PWR fuel was used. This correlation was obtained at SNL as a weighted average of commercial PWR fuel, taking into account variations in burnup and cooling time. These data are shown in Appendix A.

Fluid transport properties of both canisters and plug remain uncertain. Canisters are designed to be impermeable for some period of time after emplacement, but they can degrade and conduct water. The permeability of the seal material can be measured under laboratory conditions, but it cannot be representative due to possible cracking of the seal and the gap between seal and the host rock. For this reason permeability was varied in a range from 1x to 100x the rock permeability.

Table 2. Summary of the repository properties.

Parameter	Value
Borehole diameter	0.34 m
Emplacement zone	3 to 5 km
Boreholes spacing (pitch length)	200 m
Number of boreholes	400
Boreholes arrangement	square lattice
Canisters average thermal conductivity	0.628 W/(m·K)
Canisters average specific heat capacity	499 J/(kg·K)
Canisters average density	4405 kg/m^3
Permeability	10^{-15} m^2
Porosity	0.01

2.3.3. Physical Correlations

Equations (2.2) and (2.19) require water properties like density, heat capacity, and viscosity. These properties depend on pressure and temperature and should be implemented using a correlation or a table. In the FALCON code IAPWS-97 tables were implemented to obtain density and viscosity [31], so the same implementation was used in the present work. Heat capacity was not available in FALCON directly. However, water heat capacity enters into Eq. (2.2) multiplied by porosity ε, which does not exceed 1%. For this reason water heat capacity was approximated with a constant value of 4180 J/(kg·K).

Equation (2.26) requires the density of brine to be modified to account for the presence of solute in it. Typically polynomial functions for brine density as function of salinity and pressure are derived [32]. They usually are applicable in a narrow range of temperatures and used mostly in oceanography applications. In the present work brine density is taken as a linear combination of IAPWS-97 water density at the given conditions, and salinity [22]

$$\rho_b(P,T,S) = \rho_w(P,T) + 0.795S. \tag{2.38}$$

This implies that the effective density of water per unit volume in presence of solute is lower than the table density of pure water:

$$\rho_f(P,T,S) = \rho_w(P,T) - 0.205S. \tag{2.39}$$

3. Implementation

3.1. MOOSE Framework

MOOSE is a computational framework designed to simplify development of fully-coupled, parallel, fully implicit, nonlinear finite element codes [11, 12]. MOOSE utilizes the mathematical principle of Jacobian-free Newton-Krylov method, which requires only residual evaluations of the discretized equations, as well as having a conventional Newton solver of equations. The equations are implemented using a modular approach, in which every term of the governing equation is represented by a single kernel. Each kernel calculates residuals (for all solvers) and derivatives with respect to some of the variables (for PJFNK and Newton solvers). The values of the residuals are collected by MOOSE and passed to libmesh framework [33]. Libmesh in turn creates matrices of unknown variables which are solved with a PETSc solver [34]. Through PETSc the MOOSE framework supports parallel solution capabilities using MPI protocol. MOOSE can run efficiently on laptops, workstations, and multi-node clusters. The main advantage of MOOSE is that many activities like parallelizing, solving equations, etc. are hidden from the user. The code developer should implement kernels for equations to be solved and some auxiliary objects used for calculation. Most of the code is written in C++, however, external FORTRAN90 subroutines can be added to the code.

Originally MOOSE was used for nuclear reactor and fuel performance analysis. However, modular structure of the code allows solving many equations beyond the area of nuclear engineering. A set of equations for fluid flow, heat transport, and rock deformation was implemented to MOOSE at Idaho National Laboratories under the name FALCON. The FALCON application was used with minor changes to solve governing equations for the deep borehole repository.

3.2. Weak Form of Equations

To implement Eqs. (2.1), (2.18), and (2.33) in MOOSE they should be written in the so-called weak form [11]. Assume that a set of test functions ψ_i is defined on each element of the mesh. These can be Lagrange, Hermite or other polynomials. Then multiply the original equations without the time derivative terms by the test functions and integrate over the element domain Ω:

$$\int_\Omega \psi \nabla \cdot \left(k_{eff} \nabla T\right) d\Omega + \int_\Omega \psi q''' \, d\Omega - \int_\Omega \psi \rho_f c_f \vec{j} \cdot \nabla T \, d\Omega = 0, \tag{3.1}$$

$$\int_\Omega \psi \nabla \cdot \left(\frac{K \rho_f^{\,2}}{\mu} \vec{g} \right) d\Omega - \int_\Omega \psi \nabla \cdot \left(\frac{K \rho_f}{\mu} \nabla P \right) d\Omega = 0, \tag{3.2}$$

$$\int_\Omega \psi \left(\frac{\varepsilon D_f}{\tau} + \frac{\alpha j}{\varepsilon} \right) \nabla^2 S \, d\Omega - \int_\Omega \psi \vec{j} \cdot \nabla S \, d\Omega = 0. \tag{3.3}$$

It should be noted that all the resulting equations are scalar equations, while the original Eq. (2.1) was a vector equation with three components. All three equations contain second derivatives under the integrals. They can be reduced to the first derivatives using integration by parts:

$$-\int_{\Omega}\nabla\psi\cdot\left(k_{eff}\nabla T\right)d\Omega+\int_{\partial\Omega}\psi\left(k_{eff}\nabla T\right)\cdot\vec{n}\,d\,\partial\Omega+\int_{\Omega}\psi q'''\,d\Omega+\int_{\Omega}\nabla\psi\cdot\rho_f c_f T\vec{j}\,d\Omega- \tag{3.4}$$
$$-\int_{\partial\Omega}\psi\cdot\left(\rho_f c_f T\vec{j}\right)\cdot\vec{n}\,d\,\partial\Omega=0,$$

$$\int_{\Omega}\psi\nabla\cdot\left(\frac{K\rho_f{}^2}{\mu}\vec{g}\right)d\Omega+\int_{\Omega}\nabla\psi\cdot\left(\frac{K\rho_f}{\mu}\nabla P\right)d\Omega-\int_{\partial\Omega}\psi\left(\frac{K\rho_f}{\mu}\nabla P\right)\cdot\vec{n}\,d\,\partial\Omega=0, \tag{3.5}$$

$$-\int_{\Omega}\nabla\psi\cdot\left(\frac{\varepsilon D_f}{\tau}+\frac{\alpha j}{\varepsilon}\right)\nabla S\,d\Omega+\int_{\partial\Omega}\psi\left(\frac{\varepsilon D_f}{\tau}+\frac{\alpha j}{\varepsilon}\right)\nabla S\cdot\vec{n}\,d\,\partial\Omega-\int_{\Omega}\psi\vec{j}\cdot\nabla S\,d\Omega=0, \tag{3.6}$$

where $\partial\Omega$ is the boundary of the domain Ω and $\vec{n}$ is the normal vector to this boundary.

These equations can be rewritten using simplified notation, where $(,)$ is used for volume integrals and $\langle,\rangle$ is used for boundary integrals:

$$\left(\nabla\psi,\left(k_{eff}\nabla T\right)\right)-\left\langle\psi,\left(k_{eff}\nabla T\right)\cdot\vec{n}\right\rangle-\left(\psi,q'''\right)-\left(\nabla\psi,\rho_f c_f T\vec{j}\right)+\left\langle\psi,\left(\rho_f c_f T\vec{j}\right)\cdot\vec{n}\right\rangle=0, \tag{3.7}$$

$$\left(\psi,\nabla\cdot\left(\frac{K\rho_f{}^2}{\mu}\vec{g}\right)\right)+\left(\nabla\psi,\left(\frac{K\rho_f}{\mu}\nabla P\right)\right)-\left\langle\psi,\left(\frac{K\rho_f}{\mu}\nabla P\right)\cdot\vec{n}\right\rangle=0, \tag{3.8}$$

$$\left(\nabla\psi,\left(\frac{\varepsilon D_f}{\tau}+\frac{\alpha j}{\varepsilon}\right)\nabla S\right)-\left\langle\psi,\left(\frac{\varepsilon D_f}{\tau}+\frac{\alpha j}{\varepsilon}\right)\nabla S\cdot\vec{n}\right\rangle+\left(\psi,\vec{j}\cdot\nabla S\right)=0. \tag{3.9}$$

These equations are integrated over time using an implicit Euler method. Time integration creates an additional kernel for each equation.

Equations (3.7)-(3.9) are defined for three variables T, P, and S. Each of them can be discretized using the expansion on a set of trial functions:

$$u=\sum_{i=1}^{N}u_i\varphi_i. \tag{3.10}$$

Usually the same trial shape functions ψ_i are used as the test functions φ_i, which simplifies integration of each term of the governing equations. Substitution of expansion (3.10) to the governing equations leads to N equations for each variable and each computational cell with N unknowns u_i. Finding coefficients u_i that turn the right side of the equations into zero solves the governing equations.

3.3. Solver Types

The right hand side of Eqs. (3.7)-(3.9) is defined on each cell and each test function and can be represented as a multivariable function:

$$\vec{F}\left(\vec{u}\right)=0. \tag{3.11}$$

The value of $\vec{F}$ can be calculated for any guess $\vec{u}_i$. In this case

$$\vec{R}=\vec{F}\left(\vec{u}_i\right) \tag{3.12}$$

is generally referred as the residual vector. Reduction of the norm of the residual to zero or close to zero indicates that solution to the discretized problem has been found. In the MOOSE framework the search of the solution can be performed using two solvers: Newton solver and Jacobian-free Newton-Krylov solver (JFNK).

3.3.1. Newton Solver

Newton solver is suitable for problems in which derivatives of the kernels can be directly calculated with respect to all variables. Consider N non-linear equations [35]:

$$\vec{F}(\vec{u}) = 0. \tag{3.13}$$

Assume that $\vec{u}_n$ is the solution at iteration n. The Jacobian matrix of size $N \times N$ of this system is defined as

$$J_{ij}(\vec{u}_n) = \frac{\partial F_i(\vec{u}_n)}{\partial u_{n,j}}. \tag{3.14}$$

Then the multivariable Taylor series of Eq. (3.13) can be expressed as

$$\vec{F}(\vec{u}_{n+1}) = \vec{F}(\vec{u}_n) + \mathbf{J}(\vec{u}_n)\delta\vec{u}_n + \text{higher - order terms}. \tag{3.15}$$

If the desired solution is $\vec{F}(\vec{u}_{n+1}) = 0$ and the Jacobian matrix can be calculated directly from the current solution u_n, then the next approximation can be obtained:

$$\mathbf{J}(\vec{u}_n)\delta\vec{u}_{n+1} = -\vec{F}(\vec{u}_n), \tag{3.16}$$

$$\vec{u}_{n+1} = \vec{u}_n + \delta\vec{u}_{n+1}. \tag{3.17}$$

Steps (3.16)-(3.17) can be repeated until the residual reduces to the acceptable value.

3.3.2. Jacobian-free Newton Krylov Solver

In many multiphysics applications partial derivatives can be difficult to determine. For this reason MOOSE utilizes the JFNK approach. In this method the full Jacobian is not needed for calculation of the solution vector update $\delta\vec{u}_{n+1}$ (3.16). Instead the full solution is searched as a linear combination of several Krylov iterations on the initial guess $\delta\vec{u}_0$:

$$\vec{r}_0 = -\vec{F}(\vec{u}_n) - \mathbf{J}\delta\vec{u}_0, \tag{3.18}$$

$$\delta\vec{u}_{n+1} = \delta\vec{u}_0 + \beta_1(\mathbf{J}\vec{r}_0) + \beta_2(\mathbf{J}^2\vec{r}_0) + \beta_3(\mathbf{J}^3\vec{r}_0) + \ldots \tag{3.19}$$

where coefficients β minimize the residual. Equations (3.18) and (3.19) contain only the result of a Jacobian acting on a certain vector. Such results can be approximated as

$$\mathbf{J}\vec{v} \approx \frac{\vec{F}(\vec{u} + \varepsilon\vec{v}) - \vec{F}(\vec{u})}{\varepsilon}, \tag{3.20}$$

where $\vec{v}$ is the given vector, and ε is a small perturbation. The details of the JFNK method can be found in [35].

The JFNK method may be slow since it may require a large number of Krylov iterations (3.19). The rate of convergence can be improved if the system is preconditioned. Using right preconditioning, one replaces the matrix equation (3.16) with an identical equation

$$\left(\mathbf{J}(\vec{u}_n)\mathbf{P}^{-1}\right)\left(\mathbf{P}\delta\vec{u}_{n+1}\right) = -\vec{F}(\vec{u}_n), \tag{3.21}$$

where **P** is the preconditioning matrix. Different preconditioning matrices are available in MOOSE; however, the most efficient are physics-based preconditioners. In this approach, preconditioning matrix **P** consists of some partial derivatives of kernels with respect to the problem variables. These derivatives may be identical to the Jacobian terms in a Newton solver. However, unlike the Newton solver, preconditioned JFNK can take approximate terms with some terms missing.

3.4. Code Description

This chapter defines the classes of MOOSE which were implemented in FALCON and were modified for the deep borehole repository modeling.

3.4.1. Variables

Governing equations in weak form (3.7)-(3.9) are defined based on three independent variables temperature *T*, pressure *P*, and salinity *S*. In MOOSE they are defined in the block `Variables` of the input file. This block specifies each variable acting on certain blocks of the mesh. This means that some equations can be solved on part of the mesh. However, in the deep borehole repository modeling all variables were defined on all blocks of the mesh. The `Variables` block also defines the type of the shape functions used, as well as the scaling factors.

3.4.2. Materials

All coefficients in the weak form equations (3.7)-(3.9) other than main variables are defined in the classes of MOOSE called Materials. The resulting objects are commonly named material properties. Material properties are updated on each nonlinear iteration and can be accessed by kernels or other structures of the code.

Each Material class contains the method `computeProperties`, in which material properties calculation is performed. Each material property should be defined on each quadrature point `qp` of the mesh. For example, the following code

```
for(unsigned int qp=0; qp<_qrule->n_points(); qp++)
{
_porosity[qp] = _input_porosity;
}
```

defines material property `_porosity` for each quadrature point `qp` equal to the `_input_porosity`.

Materials structure of the original FALCON includes five Materials. The basic class is `PorousFlow`, which defines fundamental rock properties like porosity. Three more advanced classes are `HeatTransport`, `FluidFlow`, and `SolidMechanics`. They inherit the objects defined by `PorousMedia`. In addition they define all the properties required for solution of three

governing equations of FALCON for heat transport, fluid flow, and solid mechanics, respectively. The last class is called `Geothermal` and it inherits all objects from the previous three classes without adding any new objects. One of the advantages of this organization of the code is that some kernels can be used independently from the others. For example, `HeatTransport` can be used to model thermal behavior without coupling to other processes.

For the purpose of the present work only four classes `PorousFlow`, `HeatTransport`, `FluidFlow`, and `Geothermal` were used. Many classes were significantly simplified. For example, the original FALCON code used pressure-temperature and pressure-enthalpy formulations of the equations of state of water. In the present work no two-phase flow is expected. For this reason pressure-enthalpy formulation was removed from the code. All objects defined in the materials are listed in Table 3.

Table 3. Material properties

Material class	Property name	Description
`PorousMedia`	`_permeability`	Permeability
	`_porosity`	Porosity
	`_density_rock`	Rock density
	`_specific_heat_water`	Specific heat of water
	`_gravity_vector`	Direction of gravity vector
	`_gravity`	Magnitude of gravity vector
	`_salinity_diffusivity`	Diffusion coefficient of salt, Eq. (2.28)
`HeatTransport`	`_thermal_conductivity`	Thermal conductivity of rock
	`_specific_heat_rock`	Specific heat of rock
`FluidFlow`	`_compressibility_rock`	Confined compressibility of rock, Eq. (2.21)
	`_d_rho_d_s`	Coefficient 0.795 in Eq. (2.38)
	`_dens_fluid_out`	Brine density, Eq. (2.38)
	`_dens_water_out`	Water density, Eq. (2.38)
	`_visc_water_out`	Water viscosity
	`_d_dens_d_press`	Partial derivative of water density with pressure
	`_d_dens_d_temp`	Partial derivative of water density with temperature
	`_tau_water`	$\frac{K\rho_f}{\mu}$ term, Eq. (2.23)
	`_darcy_mass_flux_water`	Mass flux of water
	`_darcy_flux_water`	Superficial velocity
	`_time_old_dens_fluid_out`	Brine density, Eq. (2.38), from the previous time step
	`_time_old_dens_water_out`	Water density, Eq. (2.38), from the previous time step

3.4.3. Kernels

After all material properties are defined each kernel in Eq. (3.7)-(3.9) can be calculated on each quadrature point. Each kernel class should have a mandatory user-defined `computeResidual` or `computeQpResidual` method. For example, for temperature diffusion term $\left(\nabla\psi, \rho_f c_f \vec{j}\cdot T\right)$ the corresponding residual method is defined as

```
Real TemperatureConvection::computeQpResidual()
{
return -
_specific_heat_water[_qp]*_darcy_mass_flux_water[_qp]*_grad_test
[_i][_qp]*_u[_qp];
}
```

Here `_grad_test` is the object for the gradient of the test function $\nabla\psi$, and `_u` is the object for the main variable of the corresponding equation T. Note that the $\rho_f \vec{j}$ term is represented by a single material property `_darcy_mass_flux_water`. The rest of the kernels are constructed in a similar way. Time integration requires additional kernels, although it does not appear in the weak form of the equations. For example, the time derivative term for solute transport $\varepsilon\frac{\partial S}{\partial t}$ is represented by the following `computeQpResidual` method:

```
Real
SalinityTimeDerivative::computeQpResidual()
{
return _porosity[_qp]*_test[_i][_qp]*_u_dot[_qp];
}
```

All the kernels used are listed in Table 4. The Source column indicates the original source of the kernels used in the code. Six kernels were taken directly from FALCON with minor modifications. `HeatSource` kernel was implemented in the library of standard kernels in MOOSE. Kernels for solute transport were implemented based on standard diffusion, advection, and time derivative kernels from the MOOSE library.

A few important notes should be made regarding the implementation of certain kernels. The time derivative kernel in the pressure equation utilizes a pressure time derivative term. However, this term should not necessarily have this form. An alternative is to implement Eq. (2.18):

$$\frac{\partial\left(\varepsilon\rho_f\right)}{\partial t}+\nabla\cdot\left(\frac{K{\rho_f}^2}{\mu}\vec{g}\right)-\nabla\cdot\left(\frac{K\rho_f}{\mu}\nabla P\right)=0. \tag{3.22}$$

In this case the density time derivative is required. Density from both the previous time step and current iteration is available to the code. In this case the final form of the term implemented is

$$\frac{\partial\left(\varepsilon\rho_f\right)}{\partial t}=\varepsilon\frac{\partial\rho_f}{\partial t}+\rho_f\beta_{P,r}\frac{\partial P}{\partial t}. \tag{3.23}$$

Table 4. Kernels

Variable	Term	Kernel Name	Source
T	$\left(\nabla\psi,\left(k_{eff}\nabla T\right)\right)$	`TemperatureDiffusion`	FALCON
	$-\left(\nabla\psi,\rho_f c_f \vec{j}\cdot T\right)$	`TemperatureConvection`	FALCON
	$\left(\rho c\right)_{eff}\frac{\partial T}{\partial t}$	`TemperatureTimeDerivative`	FALCON
	$-\left(\psi,q'''\right)$	`HeatSource`	MOOSE
P	$\left(\nabla\psi,\left(\frac{K\rho_f}{\mu}\nabla P\right)\right)$	`WaterMassFluxPressure_PT`	FALCON
	$\left(\psi,\nabla\left(\frac{K\rho_f{}^2}{\mu}\vec{g}\right)\right)$	`WaterMassFluxElevation_PT`	FALCON
	$\left(\varepsilon\beta_{P,f}+\beta_{P,r}\right)\rho_f\frac{\partial P}{\partial t}$	`MassFluxTimeDerivative`	FALCON
S	$\left(\nabla\psi,\left(\frac{\varepsilon D_f}{\tau}+\frac{\alpha j}{\varepsilon}\right)\nabla S\right)$	`SalinityDiffusion`	MOOSE
	$\left(\psi,\vec{j}\cdot\nabla S\right)$	`SalinityConvection`	MOOSE
	$\varepsilon\frac{\partial S}{\partial t}$	`SalinityTimeDerivative`	MOOSE

Another concern is the stability of the advection-diffusive solution of temperature and solute transport. Unlike the pressure equation, which is purely diffusive, temperature and solute transport equations have both advective and diffusive terms. The temperature equation has diffusivity around three orders of magnitude higher than the salinity equation, so no stability issues of the solution were observed. In addition to this, mesh was refined around the borehole where the highest temperature gradients are observed.

For salinity advection, however, additional stabilization was needed. The stabilization term was added as isotropic streamline-upwind Petrov-Galerkin (SUPG) [36]. Consider the general advection problem equation

$$\frac{\partial U}{\partial t}+\vec{j}\cdot\nabla U=0. \tag{3.24}$$

on a grid with element size a. It can be derived [36] that this scheme can become stable if an artificial diffusion term is added to the equation with the coefficient of diffusion

$$D=\frac{a}{2}\left|\vec{j}\right|. \tag{3.25}$$

Eq. (3.25) ensures that numerical diffusion is adjusted for the numerical needs locally. Additional numerical diffusion is high only in the regions with large cell size a and high flow velocity j. For this reason the `SalinityConvection` kernel was implemented with an SUPG diffusion term.

Each kernel might have optional `computeJacobian` or `computeQpJacobian` method defined for it. This method creates an approximate Jacobian that can be used for preconditioning of the JFNK method or for a Newton solver. For example, the `TemperatureConvection` kernel has an approximate Jacobian term

```
Real TemperatureConvection::computeQpJacobian()
{
return -
_specific_heat_water[_qp]*_darcy_mass_flux_water[_qp]*_grad_test
[_i][_qp]*_phi[_j][_qp];
}
```

which represents the partial derivative of the term with respect to the equation variable T. Another type of optional methods is off-diagonal Jacobians. These methods represent partial derivatives with respect to variables other than that of the kernel. Off-diagonal Jacobians were implemented for the pressure time derivative kernel, since it had clear dependence on the changes of salinity and temperature in the given cell.

3.4.4. Boundary Conditions

Boundary conditions appear as surface integrals in the weak forms (Eqs. (3.7)-(3.9)). Only two types of boundary conditions were used in the deep borehole repository modeling: Neumann boundary conditions and Dirichlet boundary conditions. Both are implemented as standard boundary conditions in MOOSE. Dirichlet boundary conditions were used for fixed values, like surface temperature, pressure, and salinity. Symmetry boundaries imply no-flux conditions, which was implemented as a Neumann boundary for the corresponding variables. The bottom was set up as no-flux for pressure and salinity, and fixed geothermal flux for temperature. It should be noted that specification of the bottom boundary condition for pressure in the input file looks like

$$\left.\frac{\partial P}{\partial z}\right|_{bottom} = 0. \tag{3.26}$$

This might seem counterintuitive, since pressure gradient is hydrostatic. However, this implementation is the only correct approach, since a $\rho\vec{g}$ component is contained in the hydrostatic pressure kernel, which was not integrated by parts in the weak form derivation of (3.8), and thus, does not require any boundary condition component.

3.4.5. Initial Conditions

Initial conditions for pressure and temperature can be obtained numerically from Eq. (2.6) and (2.16). However, for the simple setup with constant properties of the rock only thermal equation (2.6) can be implemented as an analytical function. Equation (2.16) can never be expressed as analytical function due to variation in water density. For this reason before each transient a coupled steady-state problem for heat and water transport was solved. The results were

output to the standard Exodus file, which was read at the beginning of the transient step as the initial condition for the transient simulation.

In the runs with saline water the salinity equation was not modeled on the first step since salinity in the natural rock is not in equilibrium. Instead it was fixed according to Eq. (2.36) for correct account of hydrostatic pressure by brine.

3.4.6. Executioner

The executioner in MOOSE is group of the classes which specify the flow of the calculation, including the time step, adaptivity, solver types, criteria of convergence, etc. A standard `Transient` executioner provides most of the features required for modeling of the deep boreholes, including the time step reduction if the solution does not converge. However, modeling of deep boreholes differs from usual applications in time scales that have to be resolved. The deep boreholes require small initial time step in the beginning for correct capturing of the initial period of high decay heat, and large time steps at the end to be able to cover all the time period modeled (1,000,000 years). In MOOSE time step is governed by `TimeStepper` class inheriting from Executioners. The adaptive time stepper `SolutionTimeAdaptiveDT` is available which adjusts time step based on the computational time of the previous time steps. It was modified to remove the capability to reduce the time step, allowing it only to increase the time step by a small percentage (typically around 1-5%) or decrease it by 50% if solve does not converge. Time steppers are discussed in detail in Chapter 4.2.

3.4.7. Functions

Functions in MOOSE are classes which allow users to implement functions of coordinate or time to be used by materials and kernels. Two functions were implemented for modeling of the deep borehole repositories. They are decay heat equation (2.37) as function of time and initial salinity profile (2.36) as function of depth. The decay heat equation for cross-code validation with the FEHM code (Appendix A) was implemented using the built-in capability of table-defined functions.

3.4.8. User Objects

The `UserObject` system in MOOSE provides data and calculation results to other MOOSE objects. The IAPWS-97 correlation was implemented in FALCON and was the only `UserObject` used in the present work.

3.4.9. Output

MOOSE is capable of output of the full solution in the most common formats (ExodusII, Tecplot and many others), as well as single value per time step by each `Postprocessor` object. In addition to this, console output gives important information about the state of the program, convergence data like residuals, etc.

Results analysis was performed using standard tools provided in MOOSE, as well as in graphing applications Paraview and Tecplot.

3.5. Geometry and Meshing

Modeling of the complete repository can be challenging and memory-consuming. For example, modeling of one quarter of a 9×9 array of boreholes in the FEHM code required 866910 nodes even without proper resolution of the boreholes. In that setup each borehole was represented by 20 elements each 100 m long. Proper refinement of the mesh in the vertical direction at the location of thermal gradients and near the borehole can increase the number of computational cells required to model complete repository of 20×20 to a few million cells. For this reason analysis of simpler geometries has been performed.

Two simplified geometries were considered in the present work. One of them assumes that the array of boreholes is infinite (see Figure 1). This allowed reducing the geometry to a single borehole with symmetry boundaries on the planes between the boreholes. In addition to this the geometry was further reduced by the factor of 4 due to symmetry of the geometry around one borehole. The infinite array of boreholes approach is the limiting case for the large array [5, 23] and correctly predicts thermal behavior of the repository. The sensitivity of this geometry to the borehole spacing can be studied. In the limiting case of infinite spacing between boreholes the geometry represents the single borehole case. This test case was used for the cross-code validation with the FEHM code in Section 5.2.

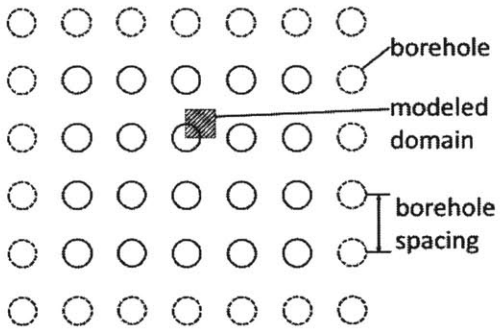

Figure 1. Infinite array of boreholes

However, one of the drawbacks of the infinite array geometry is that it does not model any sink for energy and momentum in the horizontal direction to the undisturbed rock. This can be avoided by considering a semi-infinite array of boreholes (see Figure 2). In this setup it is assumed that the array of boreholes is infinite along one of two horizontal axes, and has finite width along the other. This allows one to reduce the modeled region while keeping the possible mechanisms for transport close to the real repository.

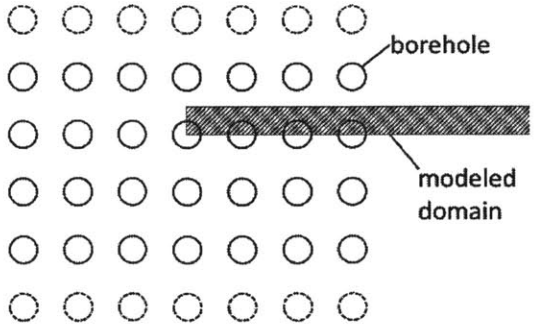

Figure 2. Semi-infinite array of boreholes

Meshing was performed using the Cubit 14.0 application [37] and exported in ExodusII file format. Meshing was performed with hexahedral elements with HEX8 type. Typically the geometry was exported as three blocks for spent fuel, seal, and rock. The meshing was always started from meshing the horizontal plane (Figure 3, left). Mesh was built using the `sizing function` capability of Cubit, which allowed gradually increasing the cell size starting from the borehole (Figure 4). All surface meshes were created using the standard `pave` scheme of Cubit. The horizontal mesh was extruded in the vertical direction using the `sweep` scheme. The mesh was created so that maximum distance between layers did not exceed 100 m. However, mesh was refined at the depth of 3 km and 5 km, where strong gradients of temperature are expected (Figure 3, right). Typically the number of the elements of the mesh for one quarter of the borehole was around 100,000.

The semi-infinite configuration was meshed similarly to the infinite array. The view of the mesh from the top is shown in Figure 5. The large part of the mesh outside of the repository is not shown in the figure. The width of the array was assumed to be 21 boreholes, so the total of ten half boreholes and one quarter borehole were meshed. The final mesh contained 769,890 hexahedral elements.

Mesh convergence has been studied on the infinite array mesh. A very coarse mesh with 25,886 elements was built as an initial mesh. It was refined two times using Cubit option

```
refine volume all numsplit 1
```

Two resulting meshes with 207,088 and 1,656,704 elements were used for mesh convergence analysis.

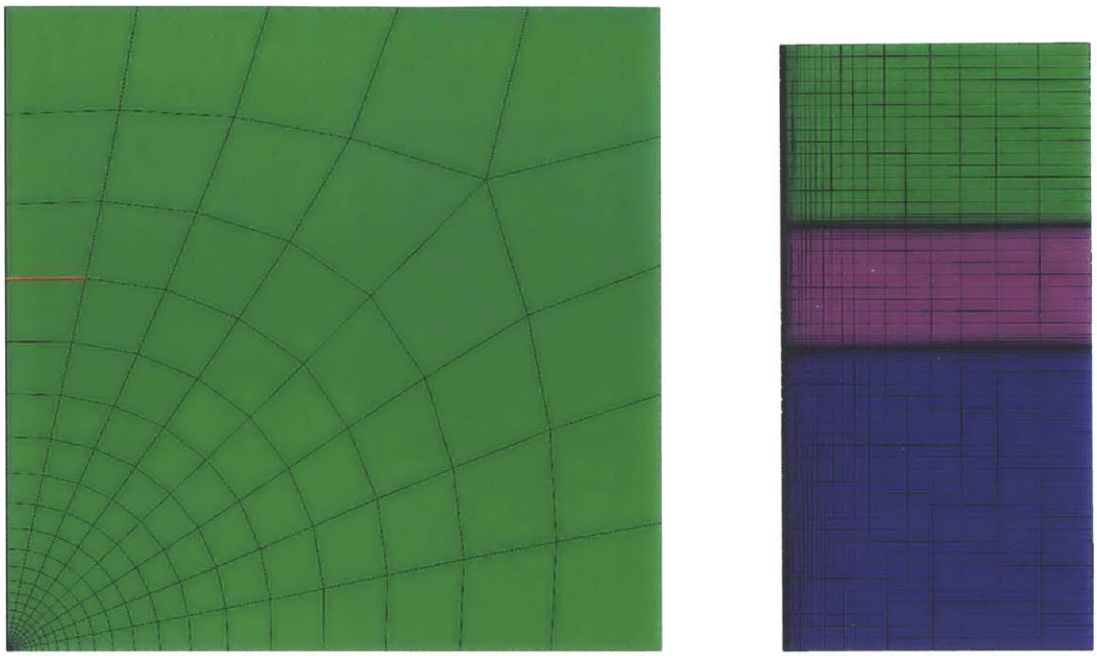

Figure 3. Mesh of the infinite array. Left: view from top. Right: view from side, not to scale.

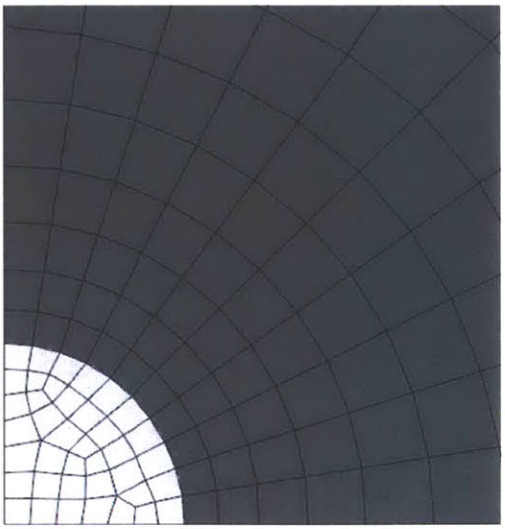

Figure 4. Close view of the mesh around the borehole.

Figure 5. Mesh of the semi-infinite array, view from top.

4. Best Practices

This chapter describes the best practices of setting up the simulation in the MOOSE environment for deep borehole repository application. This was studied on the reference case described in Chapter 2.3. The geometry was set for the infinite array configuration, which can be represented by a relatively small mesh.

Most of the runs were performed on the cluster of the NSE department of MIT. The cluster has 12 computational nodes with 24 GB of RAM on each node and Intel® Xeon® CPU E5-2620 2.00 GHz 6-cores processors (12 threads on each processor with hyper-threading enabled). The number of nodes for each simulation was taken so that the number of mesh elements per thread did not exceed 5000. This ensures efficient usage of the cluster and minimizes losses on nodes communication [38].

As a figure of merit the maximum water upward displacement was chosen. It is defined as [6]

$$z(t_0) = \int_0^{t_0} v(t)dt \tag{4.1}$$

at a certain location above the borehole. The physical meaning of this value is the maximum displacement of the water front over the time period from 0 to t_0. The maximum displacement was monitored at the depth of 1 km (2 km above the borehole) in the plug region, where the permeability is assumed to be 10 times higher than in the rock. Taking into account Eq. (2.14) which correlates seepage velocity to the superficial velocity, Eq. (4.1) can be expressed as

$$z(t_0) = \frac{\int_0^{t_0} j(t)dt}{\varepsilon}. \tag{4.2}$$

Taking into account that porosity is assumed to be a constant 1%, Eq. (4.2) becomes

$$z(t_0) = 100 \int_0^{t_0} j(t)dt. \tag{4.3}$$

The simulation time t_0 was chosen at 10^{11} s.

4.1. Solver Parameters

4.1.1. Convergence Criteria and Scaling

The goal of the solver is to reduce the residual of the weak form of Eq. (3.7)-(3.9) to zero or value which is low enough to consider that the mathematical formulation of the problem converged to the right solution. This can be done with various solver options at different performance, however, low enough residuals indicate that the solution has been found regardless of the method used.

In MOOSE one residual norm used for convergence analysis is calculated for all equations over the whole domain. For example, for the set of Eqs. (3.7)-(3.9) one can write

$$\|R\| = \sqrt{\|R_T\|^2 + \|R_P\|^2 + \|R_S\|^2}, \tag{4.4}$$

where $\|R_T\|$, $\|R_P\|$, and $\|R_S\|$ are the norms of the Eqs. (3.7), (3.8), and (3.9), respectively. However, Eqs. (3.7)-(3.9) represent conservation of energy, mass of water, and mass of solute, and have dimensions of J/(m^3·s), kg/(m^3·s), and kg/(m^3·s). Due to the dimensional nature of the individual residuals they should be non-dimensionalized or scaled.

MOOSE implements the approach of scaling. It is assumed that in order to have sufficient convergence of solution of each governing equation the residuals should be multiplied by some factors that make initial residuals at each time step of the same order of magnitude:

$$\|R\| = \sqrt{\|R_T\|^2 + (C_P\|R_P\|)^2 + (C_S\|R_S\|)^2}. \tag{4.5}$$

It was found that the best scaling parameters for the set of Eqs. (3.7), (3.8), and (3.9) are

$$C_P = 10^8, \quad C_S = 10^6. \tag{4.6}$$

These coefficients are implemented in the `Variables` block using `scaling` parameter.

The convergence criterion is governed by the parameter `nl_rel_tol`, which defines the relative decrease of the residual (4.5) required to stop the current time step or steady run. The default value of this parameter in MOOSE is 10^{-8}. However, this value should be adjusted for different simulations.

The steady state runs start with an approximate value of pressure and temperature distribution and have very high initial residual. The default value of the convergence criterion is not sufficient for the code to converge. The resulting steady state causes significant unphysical water flow in the beginning of subsequent transient simulation. For this reason the convergence criterion was reduced to 10^{-14}. The iterative process stops if the residual does not change during several iterations, so the final drop of residual typically observed during steady state was around 10^{-12}–10^{-13}.

For the transient runs convergence of the order of 10^{-8} was never achieved. Typically the best reduction of the residual was of the order of 10^{-5}. However, an insufficient convergence criterion leads to significant numerical error in the solution. Figure 6 shows the dependence of velocity as function of time for two different convergence criteria of 10^{-3} and 10^{-4}. The solution with criterion set to 10^{-3} does not converge and shows clear numerical oscillation. A quantitative measure of such oscillations is the maximum upward displacement, which is shown in Figure 7. The results converge to the value around 197 m with the error of around 1%. This error can be taken as the minimum iteration error of the simulation.

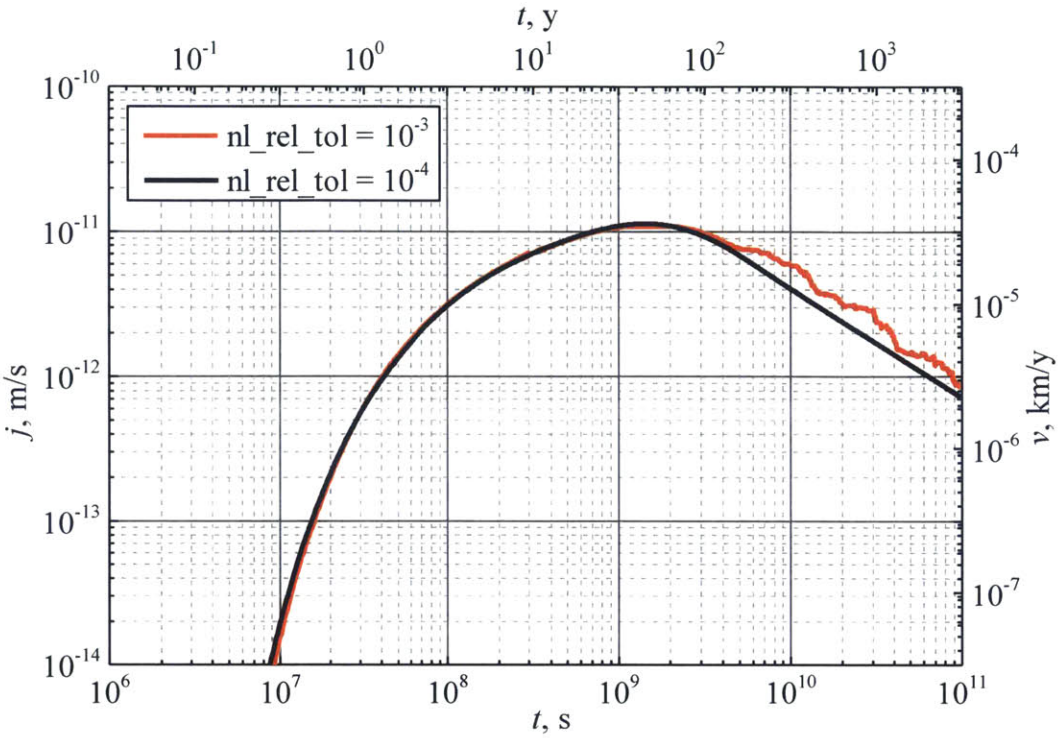

Figure 6. Velocity as function of time for different convergence criterion

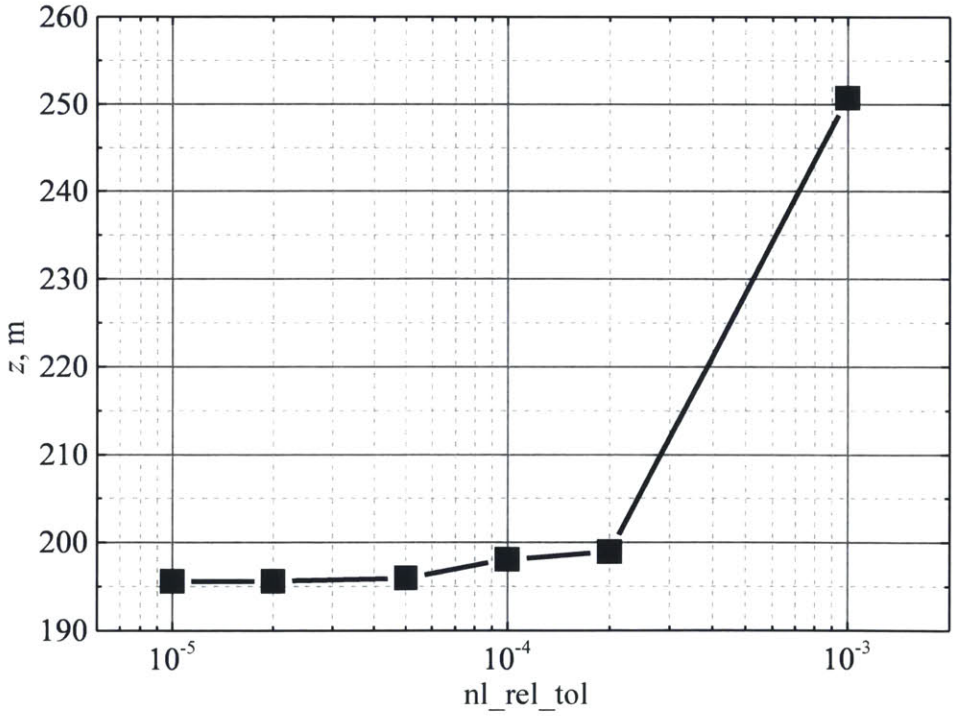

Figure 7. Maximum upward displacement as function of nonlinear convergence criterion

4.1.2. Solver Type and Preconditioning

Although the solution itself does not depend on the solver type but depends on the iteration criteria, computational time of different methods can vary by orders of magnitude. The different methods discussed in the FALCON report [31] include only the performance plots of JFNK and PJFNK solvers as a function of number of iterations. Similar analysis was performed for Newton, JFNK, and PJFNK solvers. It turned out that the JFNK solver without preconditioning never converges even for one time step of a transient problem. The behavior of the Newton solver compared to the PJFNK solver is shown in Figure 8. It is clear that convergence by the same factor takes less iterations for the PJFNK solver compared to the Newton solver.

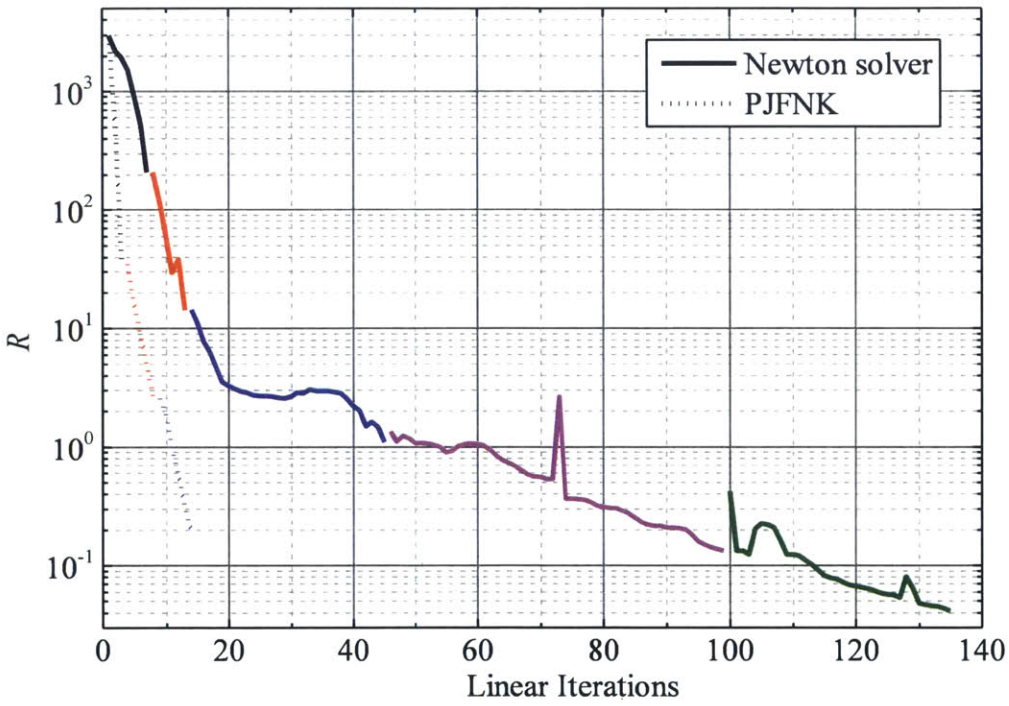

Figure 8. Performance of the solver for Newton solver and preconditioned JFNK solver with the same preconditioner (hypre). Different colors correspond to different non-linear iterations

However, a smaller number of iterations does not necessarily mean better performance in terms of computational time. Iterations of Newton method tend to be faster than iterations of PJFNK method. Two methods were studied with three different preconditioners available in MOOSE. The performance of the preconditioners was compared for the same setup for 20 time steps. The performance results are shown in Table 5. Preconditioned JFNK method with block Jacobi preconditioner failed to converge on the standard setup. The rest of the runs showed approximately the same performance for Newton and PJFNK solvers. On average the Newton solver was 3 times faster than the PJFNK solver. The best performance was obtained with block Jacobi preconditioner. This setting was used in the rest of this work.

Table 5. Performance of different solvers and preconditioners

Preconditioner	PJFNK	Newton
ASM (Additive Schwarz method)	2212 s	619 s
bjacobi (Block Jacobi)	-	488 s
hypre	1846 s	525 s

4.1.3. Shape Functions

A number of shape functions of different families and order are available in MOOSE. The most common and default functions used are Lagrange family of first order. Other functions like second order Lagrange, third order Hermite, were tested. It was found that higher orders increase the computational time significantly and do not affect the solution. First order Lagrange polynomials were subsequently used for all variables.

4.2. Time and Grid Convergence

Default adaptive time stepper `SolutionTimeAdaptiveDT` is available in MOOSE. This time stepper tries to decrease or increase time step by a small percentage (default value of 10%). The direction is chosen by the algorithm based on the processor time required to compute a previous few time steps. If the solution fails to converge the time step is decreased by a factor of 2. This time stepper was applied to the reference setup. The resulting behavior of time step Δt as a function of physical time t is shown in Figure 9 with red color.

One can see that the general trend is that time step grows on average. However, very often time stepper switches the direction of time step change and begins to decrease the time step. At least once the solution did not converge (at $t \approx 8\times10^{12}$ s) and time step dropped by the factor of 2. This behavior of time stepper was acceptable, however, time step decrease by small percentage is usually not needed during the simulation and was removed in the modification of the time stepper. The performance of the new time stepper is shown in Figure 9 with a black line. Time halving was left as the only mechanism of time step reduction and it occurred four times during the reference problem solution.

Improvement of the time stepper allowed performing a rigorous time and grid convergence study of the problem. The behavior of time step with time varies for different setups and even meshes. For this reason, convergence was studied only over the initial period of time before the first drop of time step occurs until $t_0 = 1.0\times10^{11}$ s. The time step growth factor was adjusted according to the relative size of mesh elements to preserve local CFL number. The results are shown in Table 6.

The results show that the difference between different meshes is within 2.3%. Unfortunately, it is impossible to obtain the exact order of convergence since the results for the first two runs are very close to each other. However, the difference is small enough to assume that the mesh and time step are sufficiently refined.

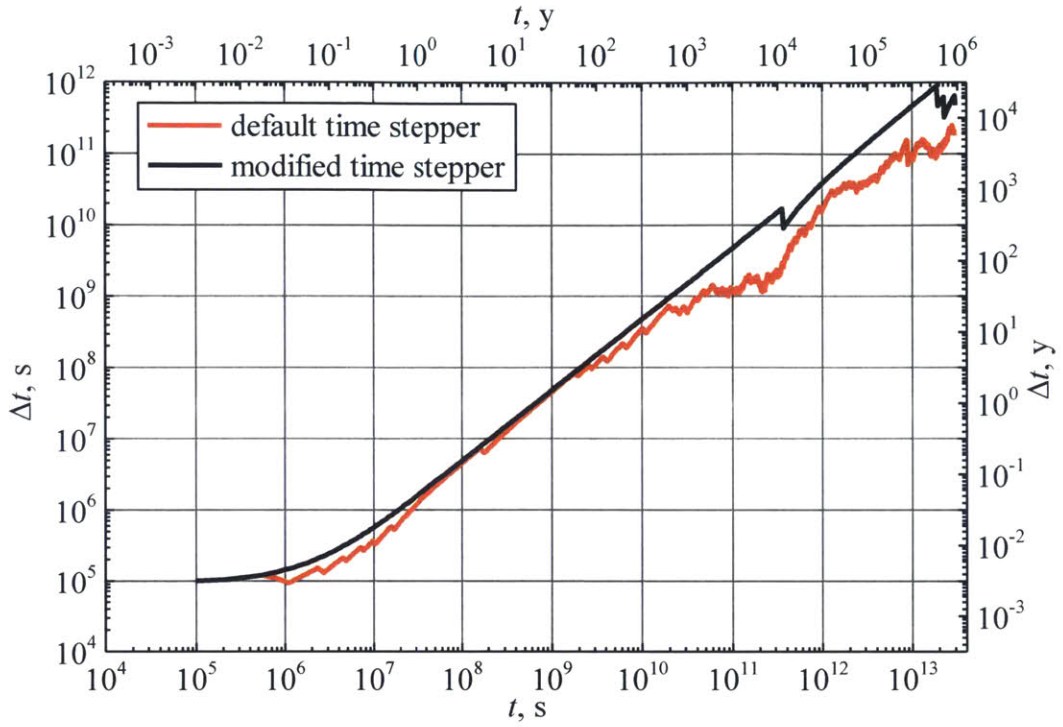

Figure 9. Time step as function of time

Table 6. Convergence analysis

Mesh relative size	Number of elements	Time growth factor	FOM, z, m
4x	25,886	0.04	195.43
2x	207,088	0.02	195.93
1x	1,656,704	0.01	200.10

5. Verification and Validation

This chapter describes verification and validation of the code. Verification was performed on the Rayleigh-Bénard convection, and validation was performed against results by Sandia National Laboratory for single borehole [23] and thermal modeling of the infinite array performed at MIT [5].

5.1. Bénard Cells Modeling

A classical benchmark for the porous thermal-hydrologic flow is the study of the critical Rayleigh number onset on convection. Consider a flat heat-conducting porous medium between two horizontal surfaces at $z = 0$ and $z = H$, and the acceleration due to gravity directed perpendicular to these surfaces. The surfaces are maintained at constant temperatures T_1 and T_2 at bottom and top, respectively. All properties of the porous medium such as density ρ_r, permeability K, heat capacity c_{eff}, thermal conductivity k_{eff}, and porosity ε are assumed constant and isotropic. The properties of the water such as thermal expansion coefficient β_T, viscosity μ, heat capacity c_f are assumed to be constant. The water is assumed to be incompressible, and the variation of density ρ_f due to any temperature change ΔT is small compared to the density.

This system is governed by the same equations (2.1) and (2.19) for heat and fluid transport as the deep boreholes repository. In the absence of water the only stationary solution for the temperature and heat flux in the medium exists similar to steady state temperature profile in rock (2.6):

$$T(z) = T_1 + (T_2 - T_1)\frac{z}{H}. \tag{5.1}$$

$$q'' = k\frac{T_2 - T_1}{H}. \tag{5.2}$$

In the presence of the water this solution is still valid, since it allows hydrostatic distribution of water pressure $P(z)$ such as superficial velocity $\vec{j} = 0$. However, this solution is not necessarily stable. A non-dimensional Rayleigh number

$$\mathrm{Ra} = \frac{K\rho_f g\beta_T H\Delta T}{\mu D_T} \tag{5.3}$$

can be introduced as a measure of the ratio of the buoyancy-driven force to the viscos force. Perturbation analysis of the steady state solution using the Fourier spectrum of the temperature solution suggests that transition from the uniform temperature to convective behavior occurs at critical number Ra_{cr} between 14.0 and 39.5 [39]. The exact critical Rayleigh number depends on the boundary conditions. They may vary between fixed temperature and fixed heat flux and permeable or impermeable wall. In the present work the bottom was taken impermeable with fixed temperature and the top was taken permeable with fixed temperature. In this case the critical Rayleigh number predicted by theory is 25.0.

The test case was set up on two-dimensional mesh with height of 1 m and width of 5 m. The side boundaries were set impermeable for fluid and heat flux. The mesh used was uniform with refinement at the top and bottom boundaries. The average temperature of the domain was

chosen at 55 °C. Temperature difference between top and bottom surfaces was chosen to minimize the effect of non-linearity of water properties. The Rayleigh number was adjusted by changing the permeability of the rock K. The summary of model parameters for the convection study is shown in Table 7.

Table 7. Convection study parameters

Parameter	Symbol	Value
Average temperature	T	55 °C
Temperature difference	ΔT	10 °C, 1 °C
Thermal expansion coefficient	β_T	4.87×10^{-4} K^{-1}
Acceleration due to gravity	g	9.81 m/s^2
Height of the domain	H	1 m
Width of the domain		5 m
Effective volumetric heat capacity	$(\rho c)_{eff}$	2.77×10^{-4} J/m^3
Thermal diffusivity	D_T	1.083×10^{-6} m^2/s
Average water viscosity	μ	5.03×10^{-4} Pa·s
Rock permeability	K	variable

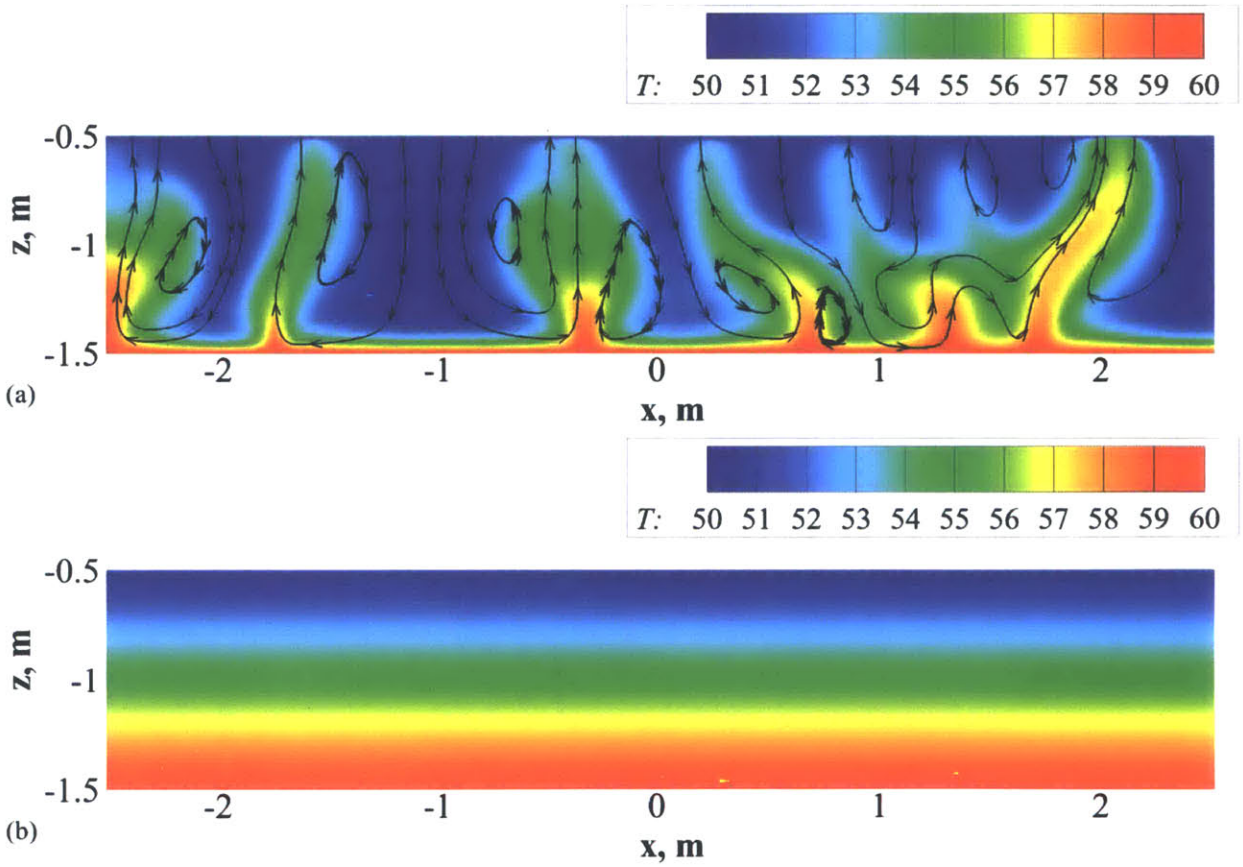

Figure 10. Temperature and streamlines at the different Rayleigh numbers. (a) Ra = 257, (b) Ra = 17

Different initial conditions were examined for modeling of the convective cells. The steady state temperature profile from Eq. (5.1) developed into convective solution, however, this process took a lot of computational and physical time (convection usually developed after $t \approx 10^6$ s. The sample result of the convection modeling for temperature difference of 10 °C and Ra = 257 is shown in Figure 10(a). The temperature field is shown with color and streamlines correspond to water flow. No steady solution was obtained, and the "fingers" fluctuated with time over the domain, splitting into new "fingers" or combining together. In contrast to this, the solution at low Rayleigh number (Figure 10(b)) remained stationary and did not change with time.

Although a convective solution was obtained at high Ra and a steady state solution was preserved at low Ra, the above approach is not practical for determination of the critical Ra. The computational and physical time required to develop convection grows while Ra approaches the critical value, which makes it impossible to run multiple test cases.

For this reason the initial setup was modified. To reduce the effect of non-linearity of water properties the temperature difference in the domain was decreased from 10 °C to 1 °C. This allowed determination of coefficients in Ra definition with better accuracy. Instead of using a uniform temperature profile (5.1) a temperature profile with small Gaussian perturbation in the middle was set as the initial condition:

$$T(z) = T_1 + (T_2 - T_1)\frac{z}{H} + T_{perturbation} \exp\left(-\frac{x^2}{C}\right). \tag{5.4}$$

Parameters $T_{perturbation}$ and C were set at 0.1 °C and 0.1 m^2, respectively. The Fourier transform of this Gaussian profile includes all possible wavelengths, including the critical one. The analysis of time dependence of temperature with time is expected to show whether the solution has unstable modes or all the modes decrease in amplitude and the whole perturbation decays with time.

The temperature of the perturbation peak was monitored in the center of the computational domain. The temperature of the steady state solution at this point was 55 °C while the initial temperature of the perturbed solution was 55.1 °C. The search for the critical Rayleigh number was performed for the permeabilities and Rayleigh numbers listed in Table 8. The temperature evolution for different test cases is shown in Figure 11. One can see that at Rayleigh number above 26 temperature increases, while for lower Rayleigh number temperature tends to decrease to the steady state value. The results in Figure 11 show that the critical Rayleigh number observed from the numerical experiment is between 19.5 and 26.0, which is consistent with the theoretical value of 25.0.

Table 8. Permeability and Rayleigh numbers in the test cases

Permeability	Ra
2.00×10^{-9} m^2	17.3
2.25×10^{-9} m^2	19.5
2.50×10^{-9} m^2	21.6
3.00×10^{-9} m^2	26.0
4.00×10^{-9} m^2	34.6

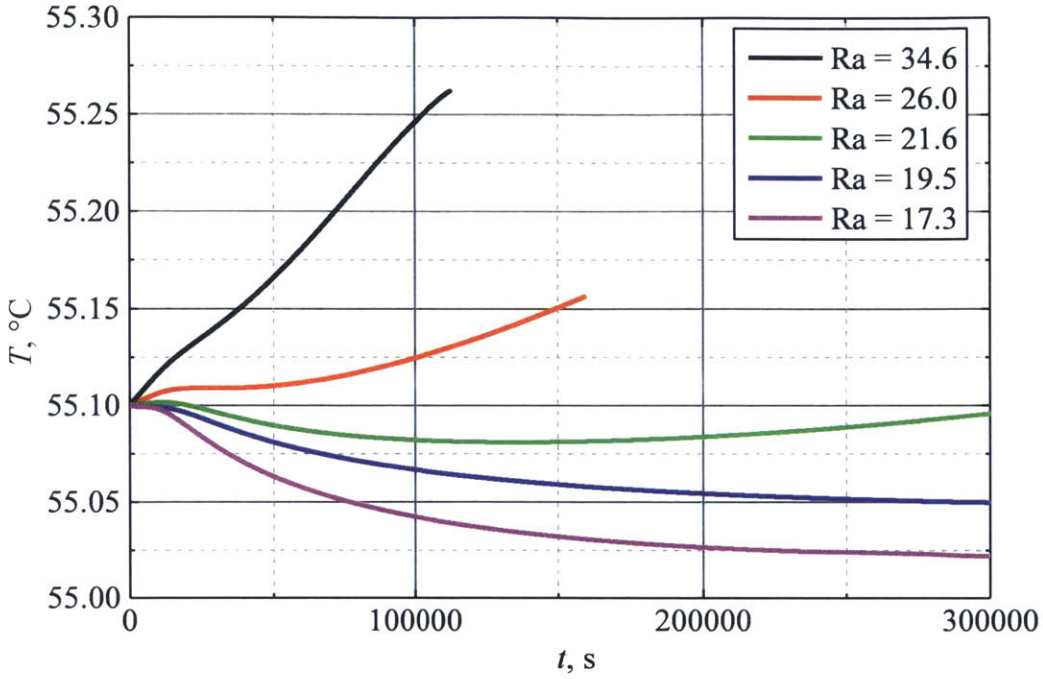

Figure 11. Evolution of the temperature of the perturbation peak for different Ra

5.2. FEHM Code Validation

A paper by Bill Arnold and Teklu Hadgu describes modeling of the coupled thermal-hydrologic processes around the deep borehole repository [23]. The geometry used included one quarter of a 9×9 array of boreholes. Heat generation was turned off on some boreholes to compare performance of 9×9, 7×7, 5×5, 3×3 arrays, and a single borehole. The last test case was chosen for cross-code validation of the FEHM code and the FALCON code. Additional data beyond those reported in the article were kindly provided by Bill Arnold.

The details of both setups are summarized in Table 9. Most of the parameters coincide with the reference setup in Chapter 2.3. However, there are certain differences. The depth of the modeled region was set to 7 km, and temperature gradient was set to 25 °C/km. The water was assumed to be fresh. The decay heat was entered as table data and is provided in Appendix A, and the total simulation time was 100,000 years instead of 1,000,000 years.

Certain parameters were different in the two setups. In the FEHM code the mesh around the borehole was square, with one element representing the borehole with effective diameter 0.88 m. In FALCON the borehole was resolved as a circle with realistic diameter of 0.34 m. This affects the behavior near the borehole and leads to sharper peaks of variables in FALCON compared to FEHM. The second difference is in the outer boundary conditions. In FEHM they were set as constant pressure and temperature, while in FALCON they were set to no flux (Neumann BS for pressure and temperature). The reason is that there is no capability in MOOSE that allows the user to fix the value of the variable during the transient run without recompiling

the code. However, the outer boundary is set far enough from the borehole so that it should not affect the solution, and this difference should have very small effect on the solution.

The results of thermal modeling in FEHM and FALCON are shown in Figure 12 and the results of fluid modeling are shown in Figure 13. Both figures show the results at the centerline of the borehole and depth of 2 km and 4 km. Figure 13 shows the superficial velocity on the left axis, and the right axis shows the seepage velocity in km/y, taking into account the porosity of 0.01 and correlation (2.14).

Thermal profiles from the two codes are consistent far from the borehole. For example, at the depth of 2 km (1 km above the disposal zone) the difference in temperature increase between the codes does not exceed 3% of the maximum temperature increase (Figure 12, top). FEHM slightly overpredicts temperature around 1000 and 100,000 years after the fuel emplacement, however, both codes predict the same magnitude and time of the thermal peak.

Table 9. Cross-code validation parameters

Parameter	FEHM	FALCON
Emplacement zone depth	3 km to 5 km	3 km to 5 km
Borehole diameter	0.88 m (effective)	0.34 m
Depth of the modeled region	7 km	7 km
Distance to the outer boundary	10 km	10 km
Surface BC	constant P, T	constant P, T
Bottom BC	no water flux, imposed heat flux	no water flux, imposed heat flux
Outer BC	constant P, T	no flux
Symmetry BC	no flux	no flux
Surface temperature	10 °C	10 °C
Temperature gradient (vertical)	25 °C/km	25 °C/km
Salinity	0 g/L	0 g/L
Decay power	Table data	Table data
Total modeling time	100,000 y	100,000 y
Rock heat conductivity	3.0 W/(m·K)	3.0 W/(m·K)
Rock heat capacity	790 J/(kg·K)	790 J/(kg·K)
Rock density	2750 kg/m^3	2750 kg/m^3
Borehole and seal heat conductivity	0.628 W/(m·K)	0.628 W/(m·K)
Borehole and seal heat capacity	499 J/(kg·K)	499 J/(kg·K)
Borehole and seal density	4405 kg/m^3	4405 kg/m^3
Borehole and seal permeability	10^{-15} m^2	10^{-15} m^2
Rock permeability	10^{-16} m^2	10^{-16} m^2
Borehole and seal porosity	0.01	0.01
Rock porosity	0.01	0.01

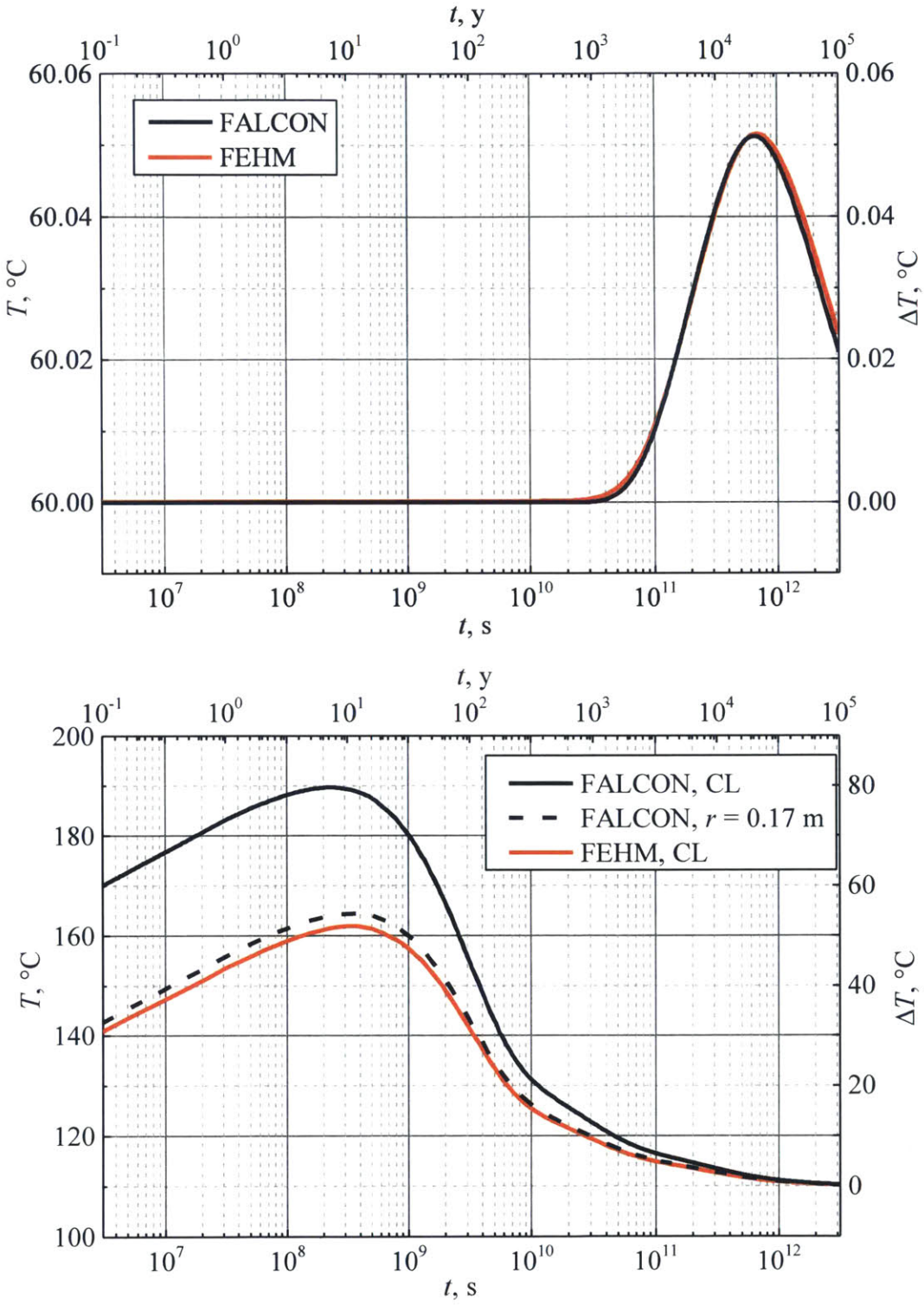

Figure 12. Semi-log plots for temperature at the centerline vs time. Top: at the depth of 2 km. Bottom: at the depth of 4 km

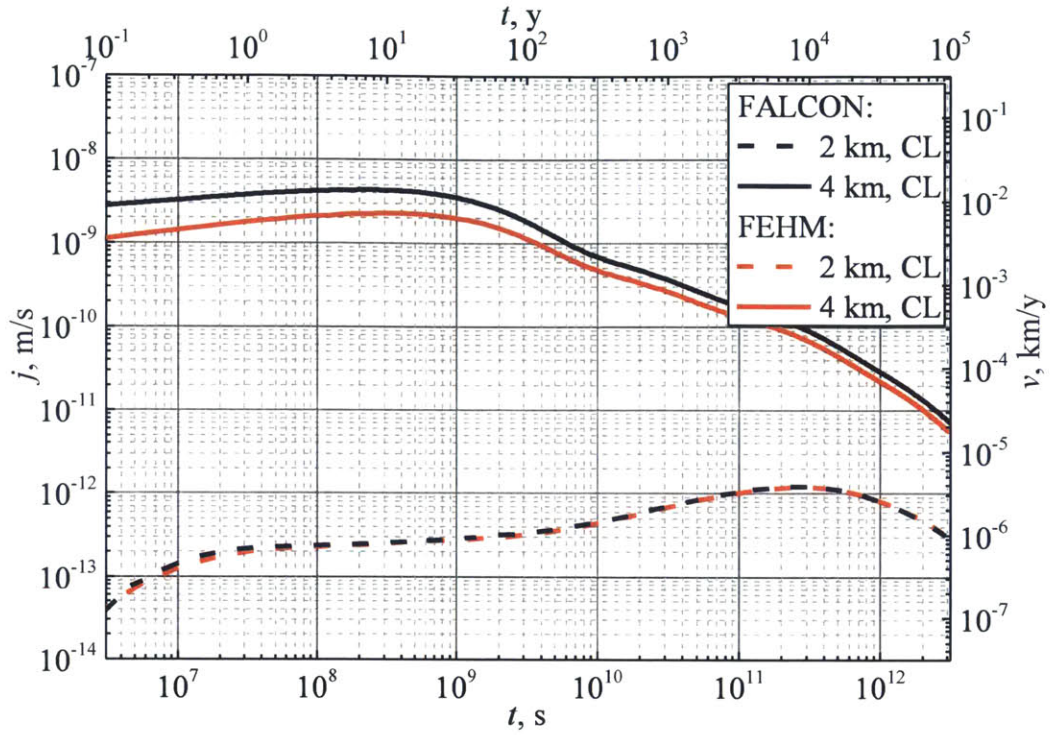

Figure 13. Log-log plots for vertical component of velocity at the centerline vs time at the depth of 2 km and 4 km

Thermal results in the emplacement zone are different for the FALCON and FEHM codes (Figure 12, bottom). Since FEHM does not resolve the borehole, the temperature in the middle cell is the average of the whole domain in the real setup. The maximum temperature in the domain at the depth of 4 km predicted by FALCON (solid black line) was up to 30 °C higher than the maximum temperature in the FEHM code (solid red line). Moreover, the canisters' surface temperature (dashed black line) was higher than the temperature predicted by FEHM.

Similar results were observed for fluid flow. The results far from the borehole at the depth of 2 km match each other within 5%, while the results in the emplacement differ by a factor up to 3. This difference is caused by the different resolution of the borehole in FALCON and FEHM discussed above, which causes higher values in the FALCON code. It should be noted that both codes represent the whole borehole as a homogeneous medium with effective porosity and permeability. Even in FALCON the velocity observed is not necessarily a real water velocity in the boreholes region.

5.3. Thermal Transient Validation

A thermal transient was validated against previous data obtained at MIT by Ethan Bates and presented at an ANS conference [5]. The test case considered in the paper included an infinite array of the boreholes with pitch lengths of 100 m and 200 m. The simulation was performed using the 2D axisymmetric diffusion solver in Matlab. For this reason the cuboid element corresponding to a borehole in an array was replaced with a cylinder with effective radius

$$R = \frac{P}{\sqrt{\pi}} \tag{5.5}$$

to preserve the area per borehole. Only heat transport was modeled, and the properties coincide with the reference setup described in Chapter 2.3. The temperature was monitored at the surface of the canister in the vicinity of the bottom of the borehole at the depth of 5 km.

The important conclusion made by the authors was that dense borehole arrangement in a repository can cause a second thermal peak at around 10,000-100,000 years after fuel emplacement. This is caused by the heat wave from the borehole reaching the symmetry boundary with the next borehole (or, in other words, reaching the opposite heat wave from the adjacent borehole). This result was later confirmed by the FEHM code for repositories of 5×5 boreholes and more [23].

The results of the modeling in FALCON compared to the 2D model in Matlab are shown in Figure 14. It should be noted that only the temperature increase with respect to initial temperature is shown. The reason for this is that in the 2D Matlab model the exact location of the point being monitored is unclear. The point was reported to be at 5 km; however, temperature increase in the first 10 years indicates that no vertical diffusion of heat occurred. The exact point was monitored slightly above the bottom of the borehole so that the temperature increase in the initial 10 years corresponded to diffusion in the horizontal plane only. In FALCON temperature increase was monitored at the depth of 4 km.

The results of thermal modeling show acceptable agreement of FALCON data with the 2D model during the first peak ($t < 100$ y). At around 1000 years after emplacement the 2D model significantly underpredicts the temperature due to heat diffusion in the vertical direction. At around 1,000,000 years the 2D model overpredicts the temperature, which can be caused by reflection of the heat wave from the bottom boundary, which was set at 8 km.

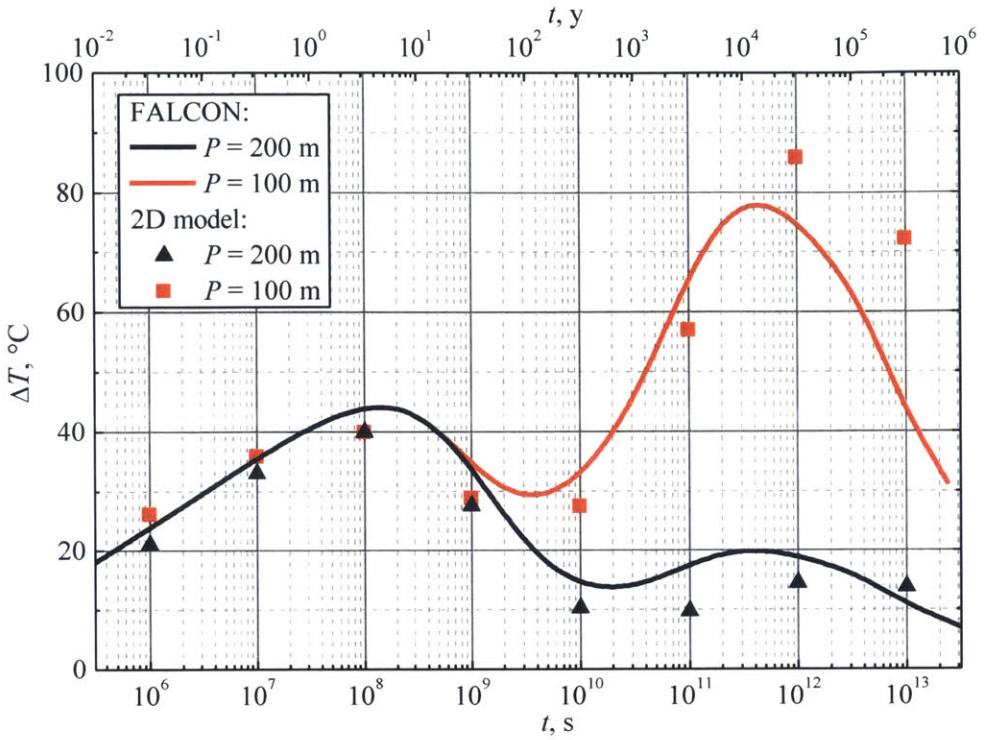

Figure 14. Semi-log plot for temperature increase at the surface of the canister vs time from the FALCON code and the 2D Matlab model [5]

6. Results

6.1. Infinite Array of Boreholes

6.1.1. Reference Case

An infinite array of boreholes represent the limiting case of a very large repository. This test case was studied using the reference parameters described in Section 2.3. In addition, this configuration was also used to develop the application best practices described in Chapter 4. For simplicity, this setup was first analyzed without the effects of salinity, which was expected to have no effect on the infinite array configuration. The thermal model was discussed in Section 5.3, and this section describes the behavior of a coupled thermal-hydrologic model.

The simulation results are shown in Figure 15 at three different times following the emplacement of the canisters containing spent nuclear fuel, which is adopted as time=0. The time dependencies of the temperature and velocity at selected locations are shown in Figure 16 and Figure 17, respectively. Similarly to the analysis of the cross-code validation, the seepage velocity is shown on the right axis.

The images in Figure 15 represent a slice of the borehole domain, starting from the borehole centerline (left) to the symmetry plane between boreholes (right). The domain is a rectangle of 100 m×10 km, where for improved visualization of the results the images are stretched in the horizontal direction by a factor of 20. The color scale represents the temperature increase of the rock relative to the initial temperature at each location. The temperature biasing allows removing the effect of the temperature difference due to the geothermal gradient, which would otherwise completely mask the changes due to decay heat. The streamlines represent the instantaneous direction of the water flow. It should be noted that streamlines do not represent quantitative displacement of water, rather they only indicate the path for the water. Since the velocity of water flow is extremely low, water is effectively only displaced a small fraction of the streamline over the whole period of 1,000,000 years.

Figure 15(a) shows the temperatures and streamlines at 10 years after the fuel emplacement. Given that the thermal diffusivity (2.10) is given by

$$D_T = \frac{k_{eff}}{(\rho c)_{eff}} = 1.38 \times 10^{-6} \text{ m}^2/\text{s}, \tag{6.1}$$

the characteristic length of temperature diffusion (2.11) is

$$L = \sqrt{D_T t} \approx 20 \text{ m}. \tag{6.2}$$

This represents the characteristic length of heat propagation from the borehole. The heat diffuses in horizontal direction from almost all regions of the borehole (except for top and bottom) due to axial symmetry and total length of the repository region (2000 m). For this region, the temperature increase is practically equal in most of the heat-generating region. At the same time, radionuclides with half-life of around 10-100 years quickly decay, leading to the decay of total power produced and therefore a decrease in the emplacement temperature. This mechanism causes the observable first temperature peak for the canisters (Figure 14 and Figure 16) at around 5 years from the initial emplacement. It is important to note that the magnitude of this peak does not depend on the spacing

of the boreholes, but instead depends on the local conditions, including thermal conductivity of the rock close to the canisters, the gap resistance between the canisters and the rock, and clearly the heat generation in the canister.

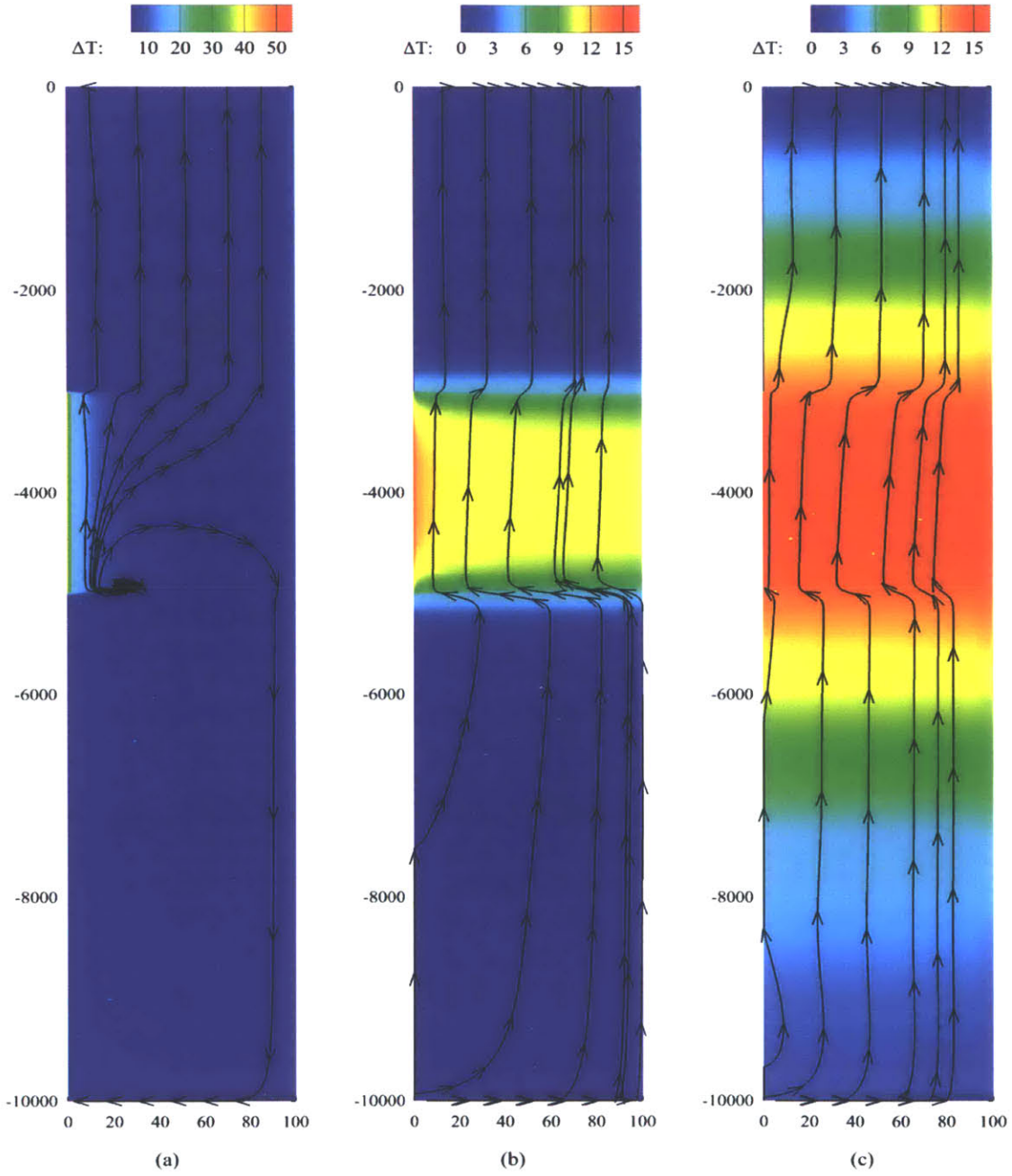

Figure 15. Temperature increase due to decay heat and streamlines of water flow caused by perturbation in the infinite array configuration (not to scale). (a) 10 years after fuel emplacement, (b) 1,000 years after fuel emplacement, (c) 100,000 years after fuel emplacement.

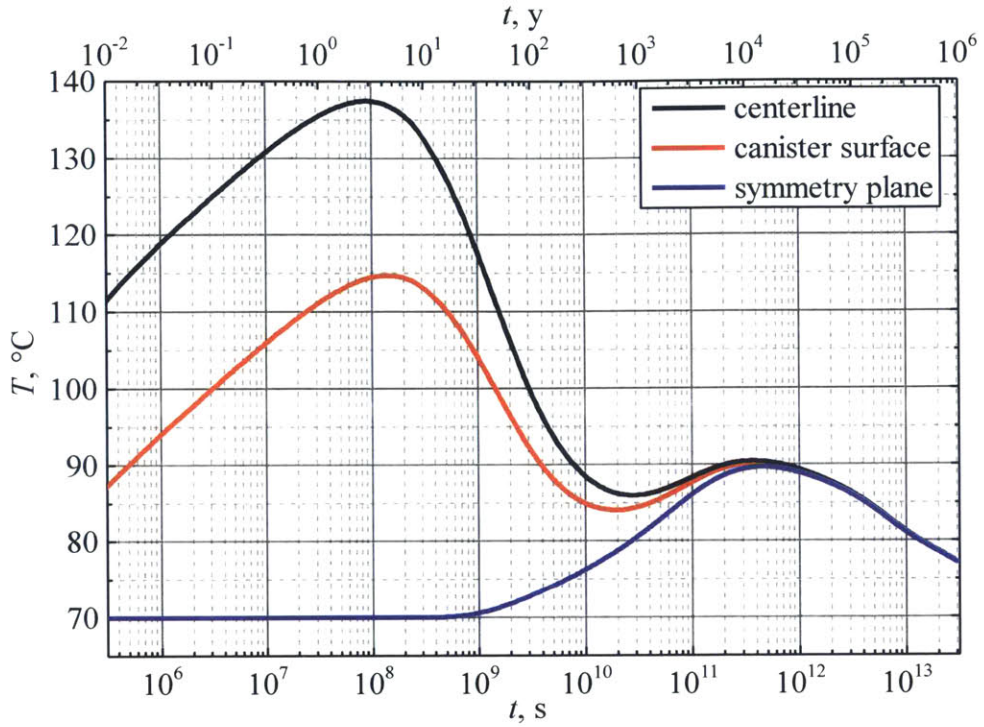

Figure 16. Temperature at the depth of 4 km as function of time for the centerline, canister surface, and the symmetry plane between boreholes of pitch length of 200 m

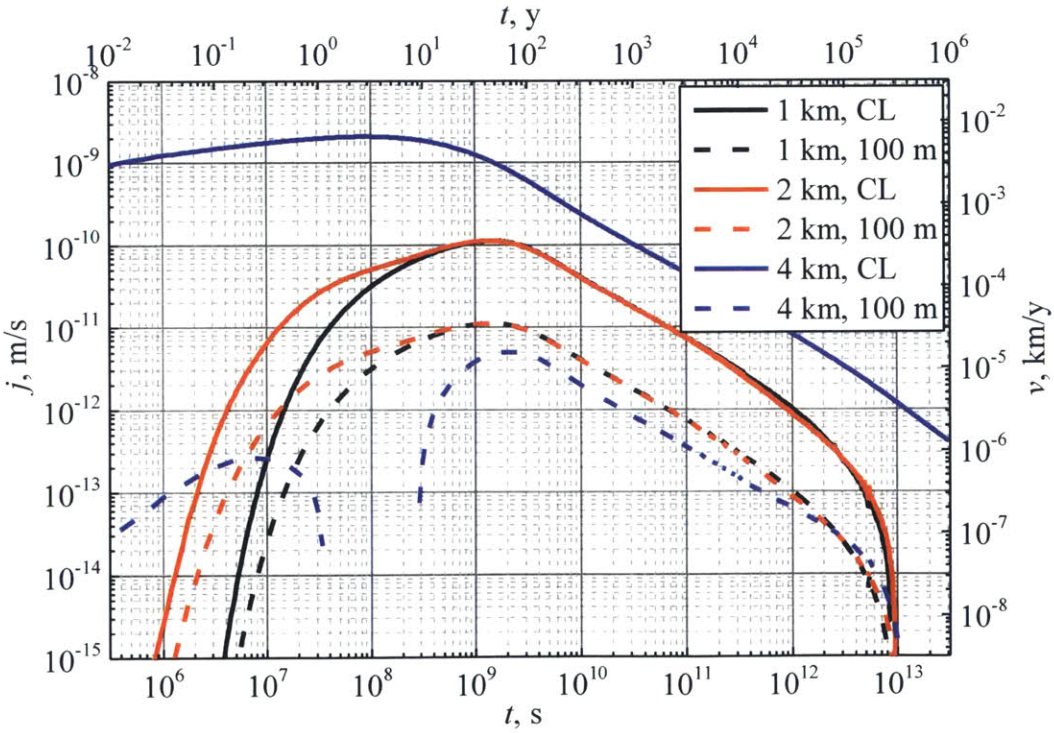

Figure 17. Velocity as function of time at the centerline and at the symmetry plane between boreholes at the depths of 1, 2, and 4 km

The water flow at 10 years from fuel emplacement is caused by the thermal expansion of the water. This wave propagates both upward and downward. However, very close to the borehole the water velocity is always directed upward due to buoyancy. The superficial velocity at the centerline in the emplacement region reaches the peak at around 5 years (solid blue line in Figure 17), while the velocity at the symmetry plane is directed downward, and is discontinuous in Figure 17 due to the logarithmic scale used. The velocity in the caprock zone reaches its peak later due to slow propagation of the water pressure wave through the rock.

Figure 15(b) shows the temperatures and streamlines at 1,000 years after the fuel emplacement. At this moment the decay power decreases significantly so that the temperature gradient close to the borehole is much lower than it was at 10 years. However, at this time the heat wave has already reached the symmetry boundary with the adjacent borehole (characteristic length of temperature diffusion is around 200 m). Depending on the spacing between the boreholes the volume of rock may be insufficient to store the heat generated at the given depth and the heat can, from this point only redistribute vertically. However, heat diffusion in the vertical direction is not sufficient to remove the extra heat in some cases and this leads to a second, delayed, increase in temperature (see Figure 16). The water flow is directed upward due to increasing average temperature of the emplacement region. Superficial velocity decreases in all regions with the slope of approximately -3/4 in log-log coordinates (see Figure 16), which is the same as the exponent in the decay heat correlation (2.37).

Figure 15(c) shows the temperatures and streamlines at 100,000 years after the fuel emplacement. At this moment the decay power of the borehole is very small so the temperature in the emplacement zone is almost uniform in the horizontal direction (see also Figure 16). The characteristic length of temperature diffusion is around 2000 m, so heat diffuses away from the borehole. At some point, this diffusive flux becomes higher than the heat generation, so the average temperature of the emplacement region decreases, and the water flow in the caprock reverses (see black and red lines in Figure 17).

It should be noted that throughout the whole transient, at each location the advective transport of heat is negligible compared to the diffusive transport. The Péclet number, which is defined as

$$\mathrm{Pe} = \frac{\rho_f c_f j \nabla T}{k_{eff} \nabla^2 T} = \frac{\rho_f c_f j L}{k_{eff}}, \tag{6.3}$$

does not exceed 10^{-2} anywhere in the geometry. This result is consistent with previous findings, which have shown that advective heat transport can usually be neglected in borehole applications [4].

6.1.2. Analytical Model

The results shown above were used by Bates to develop a simplified model of the water flow in the caprock zone of the repository [21]. Two observations lead to the development of the simplified model:

1) The flow in the caprock zone is upward and uniform at any period of time. Although there is some convection in the emplacement zone with downward water flow in the cold regions (at the symmetry plane) and upward flow in the hot region (the vicinity of

the borehole), there is no convection in the caprock. The superficial velocity in the plug region (solid black and red lines in Figure 17) is exactly 10 times higher than that at the symmetry plane (dashed black and red line in Figure 17). The permeability of the plug was assumed to be 10 times higher than that of the rock, which means that the driving pressure gradient is uniform across the horizontal plane in the caprock.

2) The superficial velocity at the depth of 1 and 2 km is the same after 10 years since emplacement, and in the interval between 100 and 100,000 years it decreases at the same rate as the decay heat (Eq. (2.37)).

To derive the equation for the superficial velocity consider the temperature and pressure diffusivities (Equations (2.10) and (2.20), respectively). The diffusivity of pressure is of the order of 0.1 m^2/s, which means that over the period of time of 10^9 s the pressure distribution should reach an equilibrium given that there are no pressure sources. However, continuing generation of heat in the canisters creates a source of pressure due to water expansion. The diffusivity of temperature is around 10^{-6} m^2/s, so one can select a region around the borehole, which does not have diffusive losses of heat over some long period of time.

Consider the region of rock around one borehole in an array below a certain boundary above the borehole (for example, this boundary can be set at the depth of 1 or 2 km). The total heat produced in one borehole is

$$q(t) = q'''(t) \cdot V_{fuel} = q'''(t) \cdot L_{emplacement} \cdot \pi r^2. \tag{6.4}$$

Define an average temperature of the rock, assuming that the specific heat capacity is constant:

$$T_{av} = \frac{\int T dV}{V_r} \tag{6.5}$$

The thermal conductivity is constant, the heat advection can be neglected, so the solution of the heat transport equation (2.1) can be represented as a superposition of a geothermal solution and a borehole solution. The overall balance of natural geothermal fluxes is zero, so they can be excluded from consideration. If all the heat generated by the radioactive decay stays in the system the average temperature changes at a rate

$$\frac{dT_{av}}{dt} = \frac{q'''(t) \cdot L_{emplacement} \pi r^2}{(\rho c)_{eff} V_r}. \tag{6.6}$$

The whole region contains a volume of water εV_r. If porosity is constant in the entire volume then the average temperature of water coincides with the average temperature of the rock. Then assuming constant properties of water the extra volume of water produced due to the thermal expansion is

$$dV = \beta_T \varepsilon V_r dT_{av}. \tag{6.7}$$

Since the pressure profile reaches steady state, it assures that all water leaves the region through the only exit to the outside, which is the top surface of the selected region with the area A. Therefore the superficial velocity through the rock is

$$j(t) = \frac{dV}{A \cdot dt} = \frac{\varepsilon \beta_T L_{emplacement} \pi r^2 \cdot q'''(t)}{A \cdot (\rho c)_{eff}}. \quad (6.8)$$

and the seepage velocity of the flow is

$$v(t) = \frac{j(t)}{\varepsilon} = \frac{\beta_T L_{emplacement} \pi r^2 \cdot q'''(t)}{A \cdot (\rho c)_{eff}}. \quad (6.9)$$

If there are regions with different permeabilities then Eq. (6.8) can be used to determine the superficial velocity in the dominating region, since the cross-sectional area of rock of 40,000 m^2 significantly exceeds the area of the plug (approximately 0.09 m^2). Since the driving pressure gradient in the seal and the rock is the same, then the velocities in the seal can be defined as

$$j(t) = \frac{K_s}{K_r} \cdot \frac{\varepsilon \beta_T L_{emplacement} \pi r^2 \cdot q'''(t)}{A \cdot (\rho c)_{eff}}. \quad (6.10)$$

$$j(t) = \frac{K_s}{K_r} \cdot \frac{\beta_T L_{emplacement} \pi r^2 \cdot q'''(t)}{A \cdot (\rho c)_{eff}}. \quad (6.11)$$

Equations (6.8)-(6.11) are valid only if general assumptions for the heat and fluid transport are valid, and only in a certain time range. Right after the fuel emplacement the pressure wave does not reach the location being monitored, and the model overpredicts the velocity. Then the model fails at around 100,000 years after emplacement due to heat diffusion away from the repository. The comparison of the analytical model to the numerical modeling is shown in Figure 18.

The analytical model allows calculating the maximum upward displacement (4.1) based on the seepage velocity (right axis in Figure 18). In the reference setup the maximum upward displacement of water in the rock is 30 m, and in the plug it is 300 m for the seal permeability of 10^{-15} m^2 (reference case) and 3000 m for the seal permeability of 10^{-14} m^2 (failed seal case in [21]). The analytical model predicts conservative fluid flux in the caprock compared to the numerical modeling since it overpredicts the superficial velocity at the time when it is not valid. However, it is not necessarily conservative if the assumptions of the infinite array (impermeable lateral boundaries) are not valid.

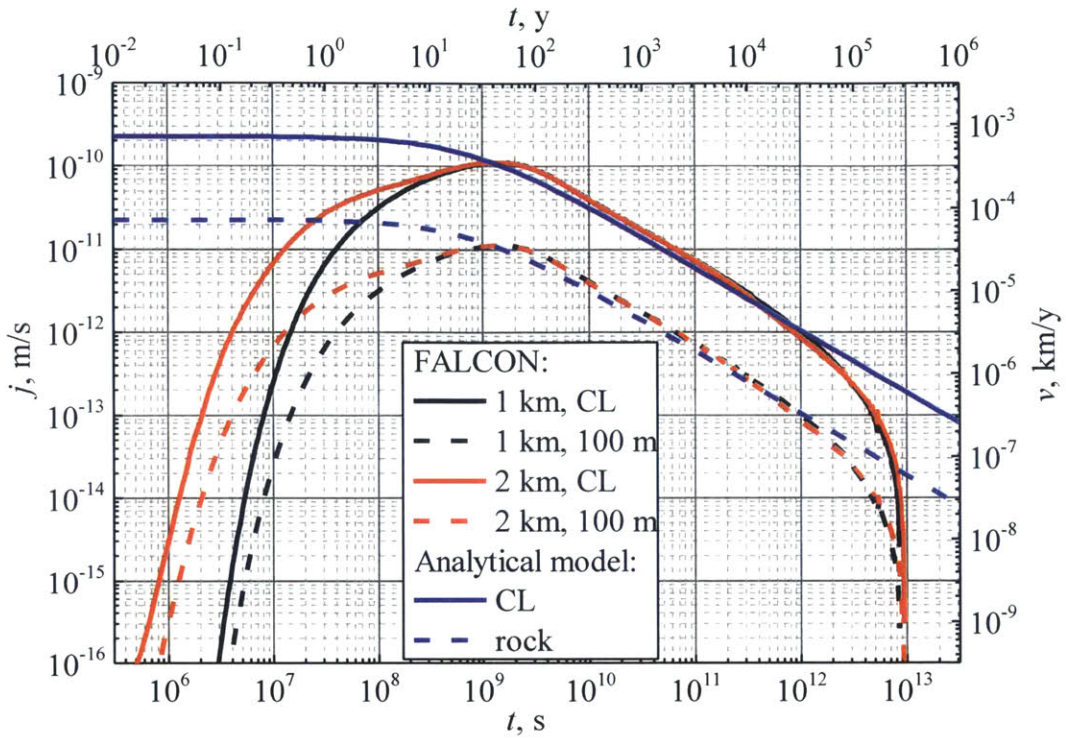

Figure 18. Velocity as function of time in the seal (centerline) and in the rock from FALCON code and from the analytical model

6.1.3. Parameters Sensitivity

The analytical model derived by Ethan Bates [21] is not sensitive to a number of parameters. For example, the superficial velocity does not depend directly on permeability, although it enters the definition of pressure diffusivity, which affects the range of applicability of the model. The seepage velocity, which defines the maximum upward displacement as the figure of merit of borehole performance, does not depend on both permeability and porosity. The analytical model does not depend on the arrangement of the boreholes (since only the area per borehole is important), or geothermal flux, rock compressibility, or salinity of water.

Nevertheless, some of these parameters can affect the results of the modeling in FALCON. This section briefly summarizes sensitivity to these results. The same data were examined in Section 4.4 of the thesis by Ethan Bates [21].

6.1.3.1. Arrangement of the Boreholes

The effect of spacing was analyzed using the discussed reference configuration and varying the different pitch length, as well as evaluating a hexagonal lattice of boreholes. For the hexagonal lattice the spacing between the boreholes was set to

$$P = 214.9\ \text{m} \tag{6.12}$$

to conserve the area per borehole at 40,000 m^2. The results for the superficial flux in the caprock region coincided with the reference square lattice results (Figure 17) and are not shown here.

The pitch length affects the borehole performance, as predicted by the analytical model, and the velocity in the caprock is inversely proportional to the square of the pitch length. The superficial velocity in the caprock near the seal at the depth of 1 km is shown in Figure 19. The profiles for pitch lengths up to 1500 m are consistent with the analytical model. However, for the case with pitch length of 3500 m a second peak is observed, which is caused by the convection in the caprock. It should be noted that this test case was run without accounting for water salinity, and the seepage velocity does not exceed 10^{-8} km/y at the second peak, leading to the maximum upward displacement of the order of 10^{-2} km. However, this result indicates that the analytical model is valid only for very tall and narrow geometries, and it is not directly applicable to wide geometries.

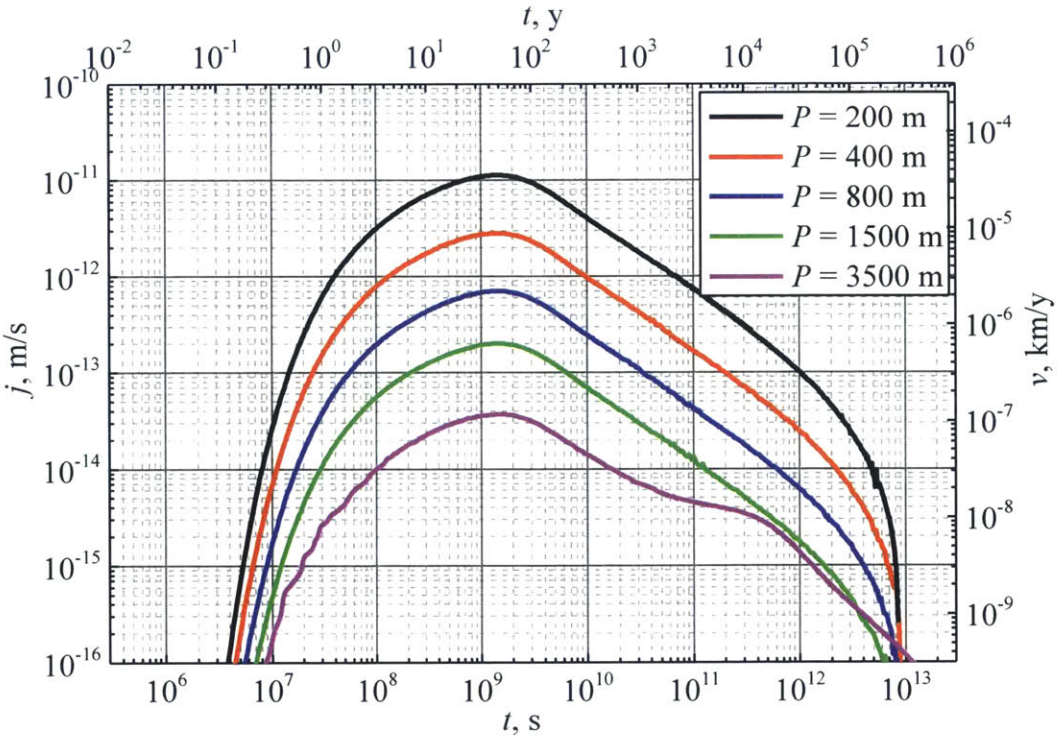

Figure 19. Velocity as function of time in the caprock at the depth of 1 km for different borehole spacing

6.1.3.2. Variations of the Power

The analytical model predicts that the water flow is proportional to the power generated per borehole. The results of the modeling in FALCON for the power at 50% and 200% of the reference case decay heat of the canisters are shown in Figure 20. The results are proportional to the decay power and justify the assumption of the superposition of different solutions made in the analytical model derivation.

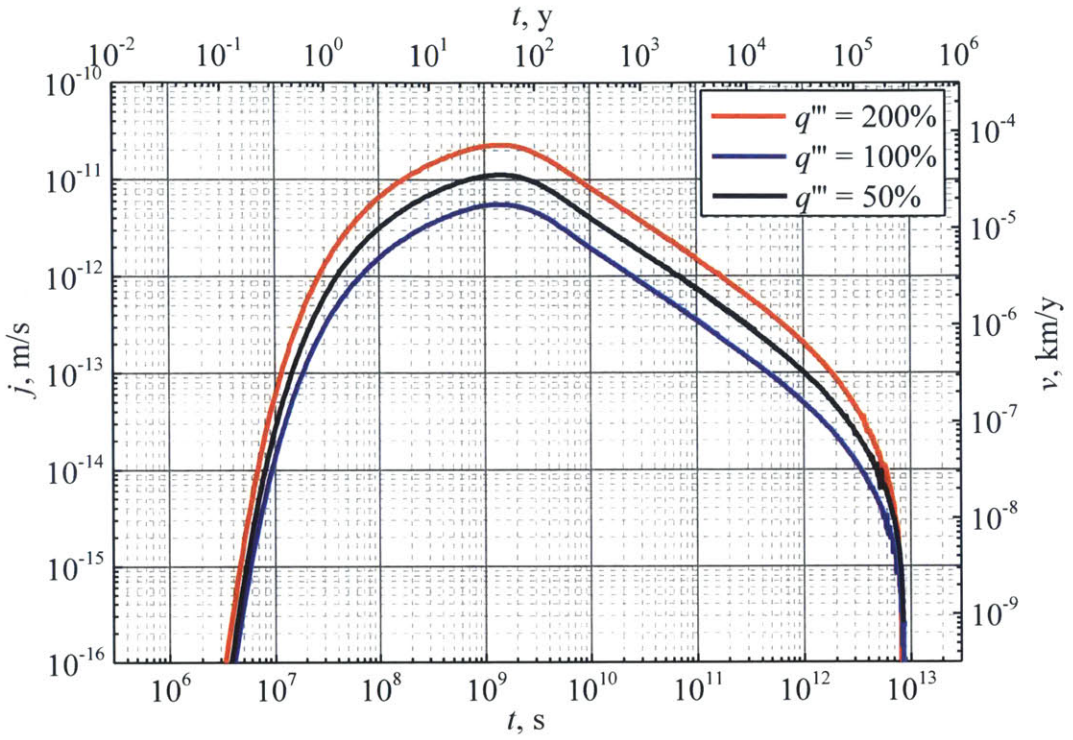

Figure 20. Velocity as function of time in the caprock at the depth of 1 km for different powers

A further test case was evaluated on the modified geometry, in order to assess the effects of different canisters in each borehole. The real borehole repository may be used for disposal of fuel from different facilities with different age and burnup. The canisters can therefore produce considerably different average decay power which could lead to unexpected temperature and consequent flow redistribution. In order to assess the performance of such configurations it was assumed that the boreholes with the decay power of 50% and 150% are arranged in the alternating rows in an infinite array. In this case the simplest modeled domain (see Figure 1) should be doubled in comparison with the previous analysis, to provide a minimum computational unit.

The results of the simulation indicate that no variation of superficial velocity in the caprock was observed across the domain. The superficial velocity in the spent fuel zone and in the caprock is shown in Figure 21. It can be observed that the velocities in the borehole depend on the heat generation of the particular borehole, however, the caprock superficial velocity is the same as for the reference setup. This indicates that the infinite array approximation can be used for modeling of boreholes with different heat generation by using the average decay heat.

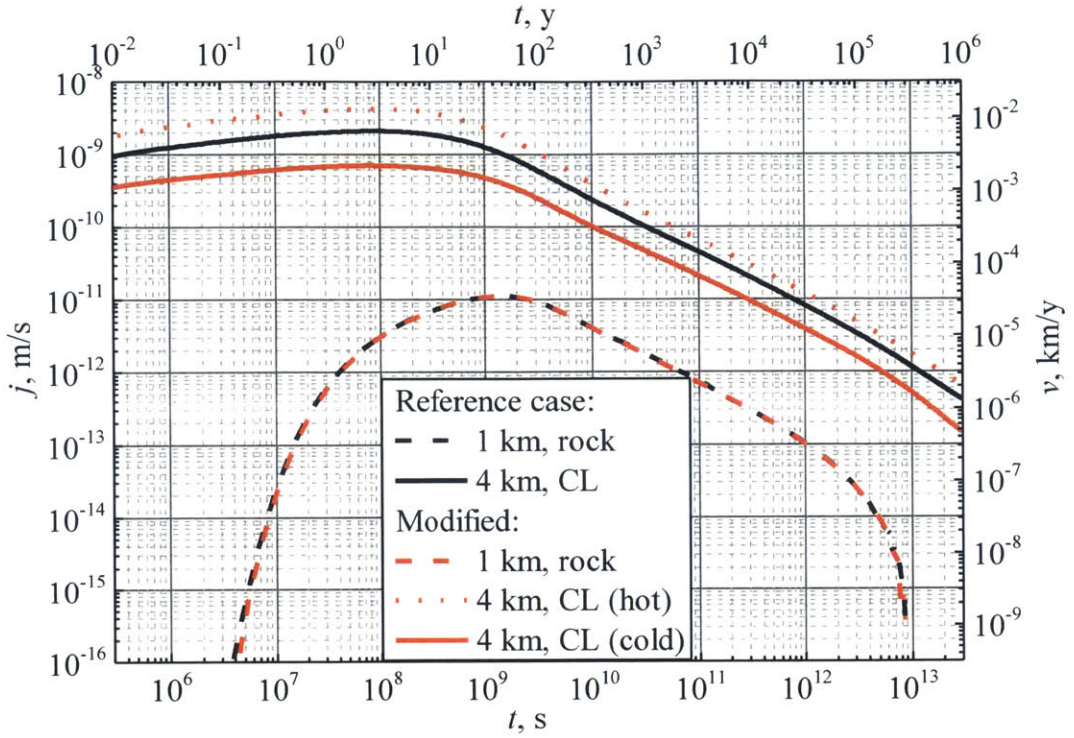

Figure 21. Velocity as function of time for the reference setup and a modified case of alternating boreholes with power at 50% and 150% of the reference power

6.1.3.3. Rock Properties

As previously mentioned, the analytical model is not sensitive to the rock permeability. However, the permeability of the rock affects the pressure diffusivity (2.20), with lower permeability corresponding to lower pressure diffusivity. This affects the time required for pressure wave to reach the point being monitored. A similar effect on the pressure diffusivity is produced by the compressibility of the rock (see equation (2.24)). The two effects are compared in Figure 22 for permeability of 10^{-16}, 10^{-17}, and 10^{-18} m^2, and the confined compressibility of rock of 4.62×10^{-12} Pa^{-1}. The results are consistent with the expected behavior.

Another important effect of the permeability and rock compressibility is the overpressure created by the water expansion in the borehole. The pressure for the same test cases at the depth of 4 km in the borehole is shown in Figure 23. Higher permeabilities tend to cause lower pressure increase, and vice versa. The overpressure might be an important factor for the mechanical failure of the boreholes and has to be considered in possible failure scenarios.

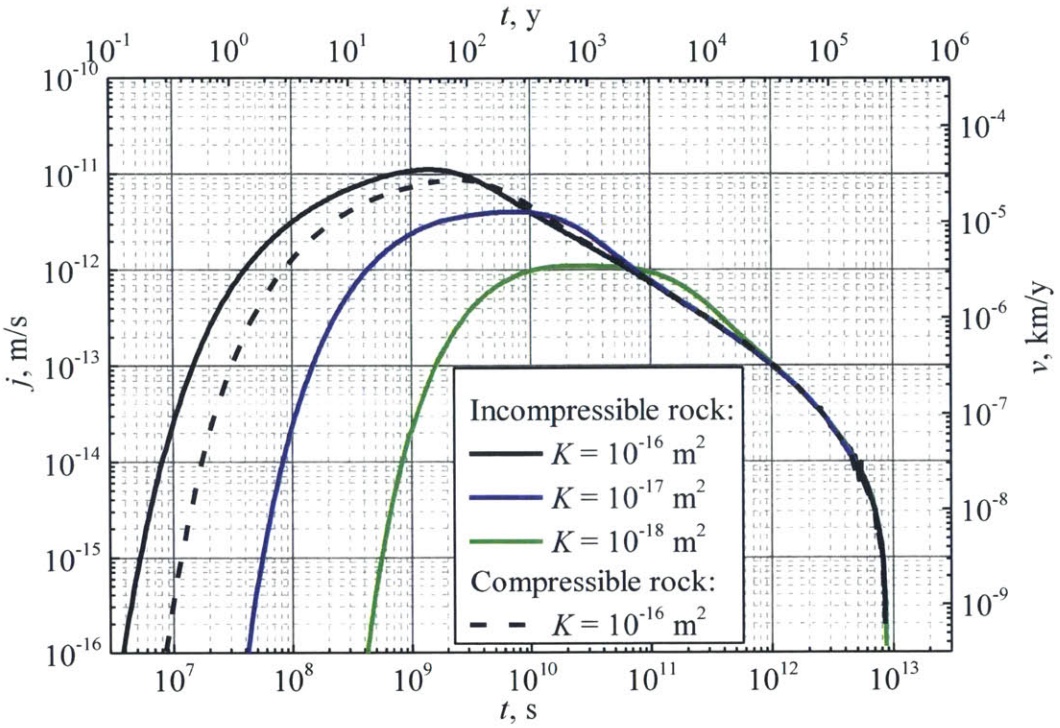

Figure 22. Velocity as function of time in the caprock at the depth of 1 km for different permeabilities and for the case with compressible rock

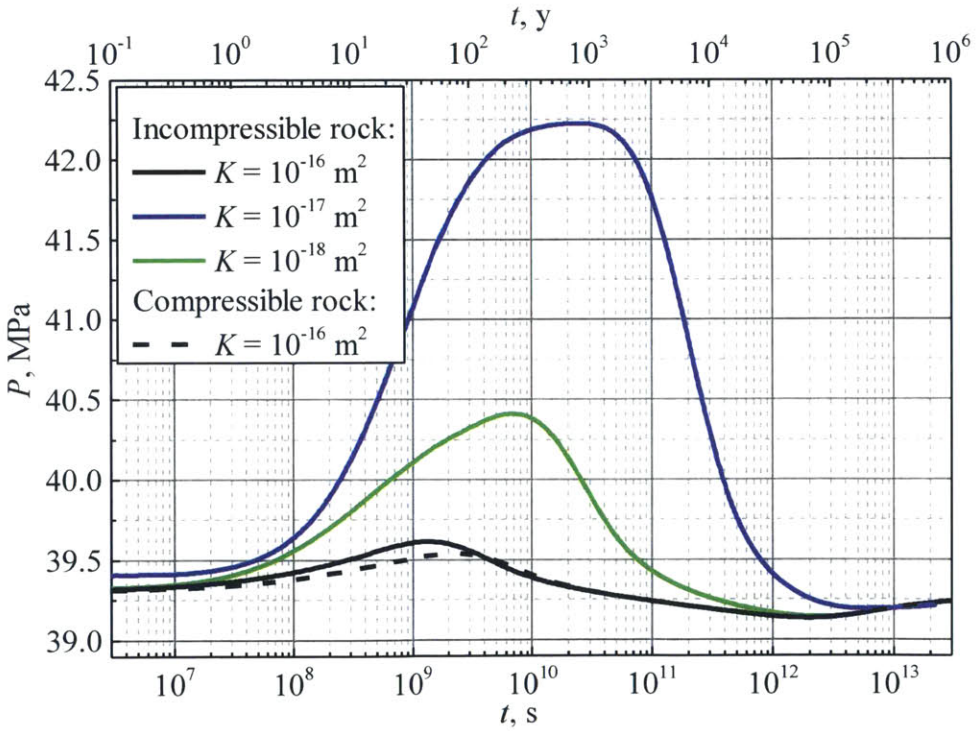

Figure 23. Pressure as function of time in the borehole at the depth of 4 km for different permeabilities and for the case with compressible rock

It should be observed that all the cases analyzed assumed constant rock permeability. In reality, rock permeability decreases with depth. Correlation (2.34) describes one of the attempts to create a correlation of permeability with depth. To remove an unphysical infinite increase of permeability, its value near the surface is limited at 10^{-14} m^2. This correlation was used in the infinite array configuration and the results were compared to the reference case (Figure 24). The resulting shape of the superficial velocity with time is slightly different in the beginning of the simulation, but coincides in the region of applicability of the analytical model.

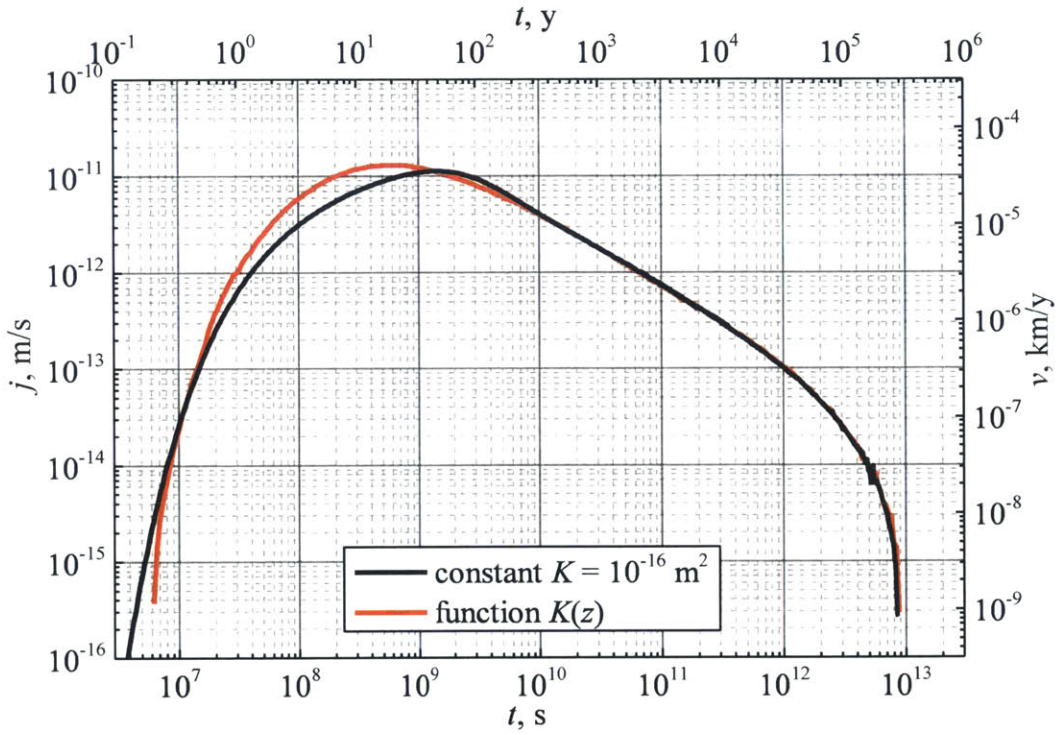

Figure 24. Velocity as function of time in the caprock at the depth of 1 km for constant permeability compared to variable permeability

A further test case was performed assuming higher permeability of the plug due to crushing of the material in the seal, or other similar failure mechanism. In this case the reference permeability of the plug was increased by the factor of 10 to 10^{-14} m^2. The results are shown in Figure 25. As expected, the variation of permeability in the plug does not affect the velocity in the caprock but increases the superficial velocity in the plug itself proportionally to the plug permeability. It should be noted that the test case with different permeabilities poses a numerical challenge and leads to slower convergence due to variation in pressure diffusion coefficient.

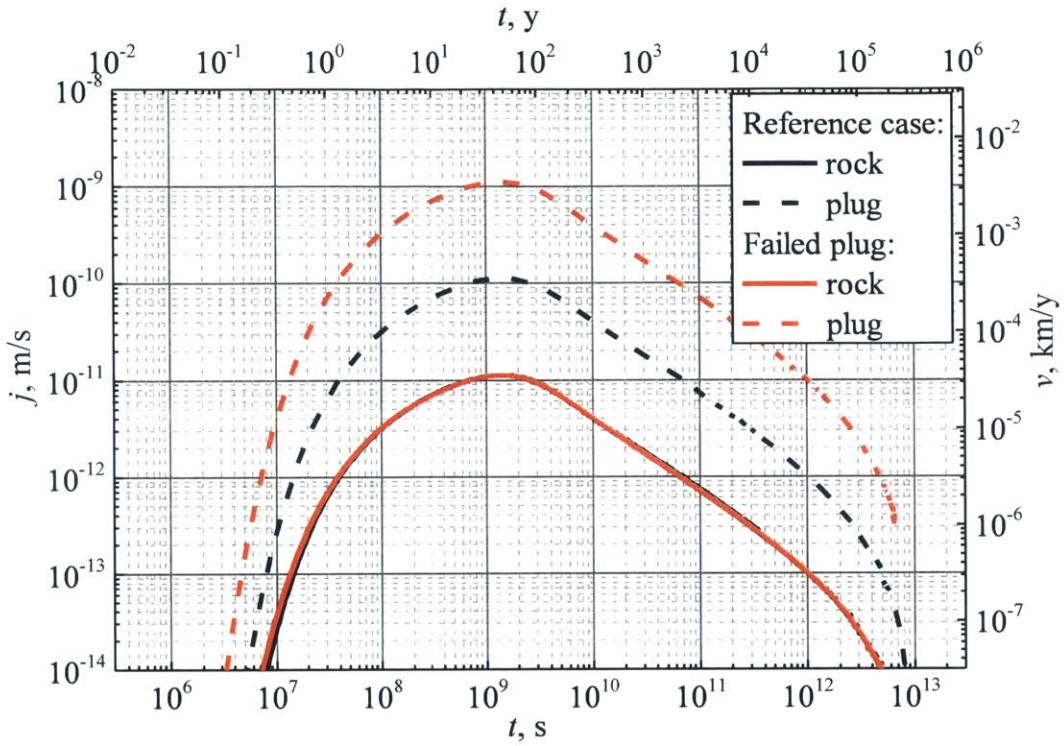

Figure 25. Velocity as function of time in the caprock and plug at the depth of 1 km for different plug permeabilities

6.2. Semi-infinite Array

6.2.1. Fresh Water

The results of the infinite array model show that no convection occurs in the rock above the emplacement zone in the reference setup. However, at the pitch length of more than 1,500 m the velocity does not follow the decay with the -3/4 slope in log-log coordinates after 10,000 years since fuel emplacement. This is caused by convection between the heated region and the bulk of the colder rock outside of the repository, although the resulting seepage velocity is too small to cause any significant upward displacement of water. A similar effect can happen on the boundary between the array of many boreholes and the undisturbed rock. In this case, the average temperature in the array should be higher than the average temperature around one borehole, as in the case with pitch length of 3,500 m, and the water velocity can be higher.

Modeling a semi-infinite array, which takes advantage of the quarter symmetry and models a 20×20 borehole array is still extremely computationally demanding. However, the effect of the convection between the repository and the surrounding rock can be studied on the semi-infinite configuration, as described in Section 3.5 (see Figure 2).

The modeling was performed using the reference parameters described in Section 2.3. Since the higher permeability of the plug had no effect on the water transport in the infinite array, the plug permeability was assumed to be the same as the permeability of the rock, in order to

improve the convergence of the code. Two rock permeabilities of 10^{-16} m^2 and 10^{-17} m^2 were studied. Pure water properties were assumed, and the salinity transport was neglected.

The semi-infinite array demonstrated poor numerical convergence when compared to the infinite array; this is related to the challenges in preconditioning this larger model. The poor numerical convergence requires reducing the simulation time step, which could not exceed in this case 2×10^{10} s. The dependence of time step on time is shown in Figure 26. At the same time each time step also requires a larger number of non-linear iteration, therefore resulting in simulations that could not be completed for the full 1,000,000 years time span.

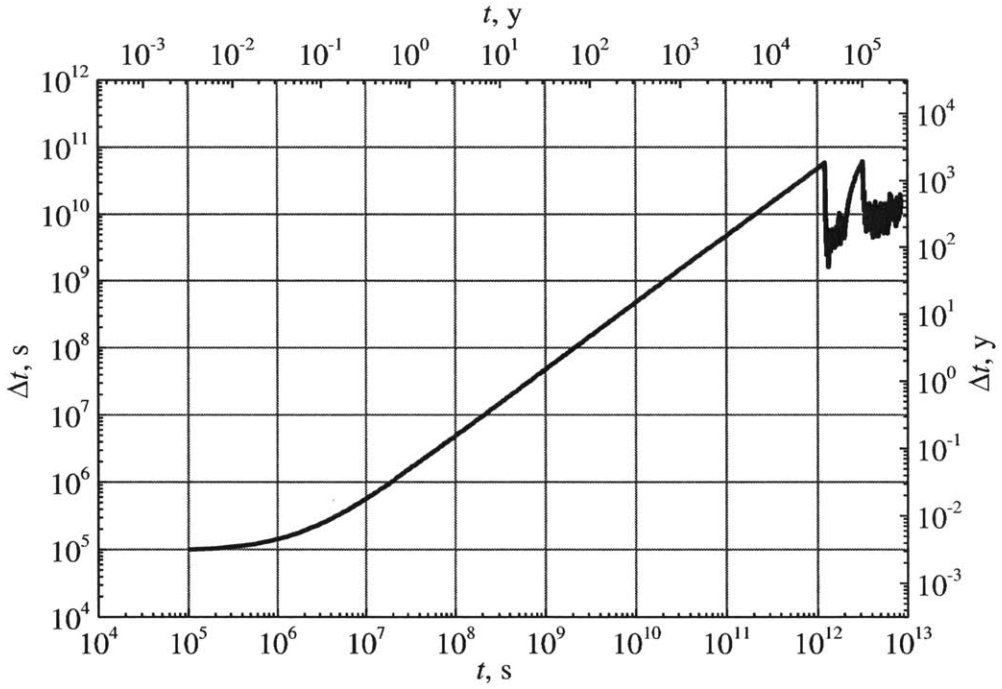

Figure 26. Time step as function of time for the semi-infinite array case

The simulation results are shown in Figure 27 at three different times following the emplacement of the canisters, for a rock permeability of 10^{-16} m^2. Similarly to the infinite array (Figure 15), the temperature increase is shown on the color scale, and superficial velocities are used for streamlines. The array of boreholes is located at the left border of the images and is represented by the 11 vertical lines in Figure 27(a).

Figure 27(a) shows the temperatures and streamlines at 10 years from the fuel emplacement. The temperature field near each borehole is the same as in the infinite array since the short-term behavior of the two setups is identical. However, the streamlines are different. The pressure wave propagates in all directions away from the repository, and so flows the water. The streamlines in Figure 27(a) end at approximately 20 km from the borehole, since the pressure wave just reaches this location and the velocity far from the borehole is close to zero.

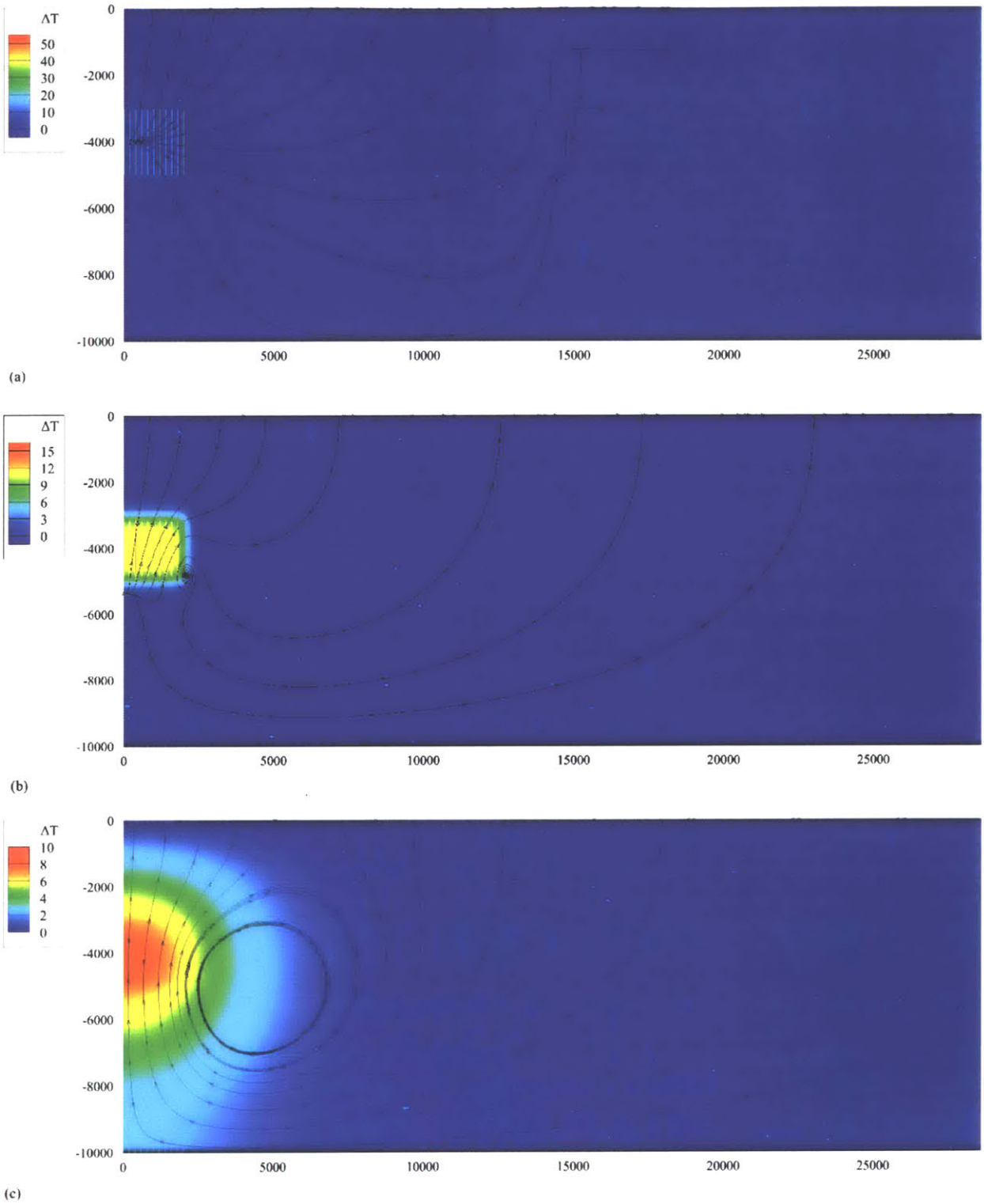

Figure 27. Temperature increase due to decay heat and streamlines of water flow caused by perturbation in the semi-infinite array configuration with rock permeability of 10^{-16} m^2. (a) 10 years after fuel emplacement, (b) 1,000 years after fuel emplacement, (c) 100,000 years after fuel emplacement.

Figure 27(b) shows the temperatures and streamlines at 1,000 years from the fuel emplacement. The maximum temperature is reduced and the emplacement zone is approximately 10 °C higher than the pre-emplacement temperatures. However, the heat generation still produces significant overpressure and the flow is still driven by expansion away from the repository. At 100,000 years from the fuel emplacement (Figure 27(c)), the behavior of the flow changes significantly. The emplacement region is uniformly heated, but the decay power is too low to cause significant expansion-driven flow. The water in the repository is warmer and causes lower hydrostatic pressure. This creates convective flow, which begins at the surface far away from the borehole, propagates to a depth of more than 5 km, passes through the emplacement region and exits the surface above the repository.

It should be noted again, as for the infinite array case, that the streamlines do not represent the real displacement of water since the velocity is low and the distance is short compared to the streamlines length (~ 40 km). However, in the semi-infinite array the water flow in the caprock is higher at the scale of 100,000 years. Figure 28 shows the superficial velocity with time in the caprock above the center borehole of a semi-infinite array compared to the infinite array in log-log scale. The superficial velocity in the beginning is lower than that in the infinite array, however, after 1000 years it becomes higher due to convection. This results in maximum upward displacement of 2,390 m in the first 250,000 years for the permeability of 10^{-16} m^2. Reduction of the permeability to 10^{-17} m^2 reduces the velocities and the maximum upward displacement becomes 987 m over the first 250,000 years. However, this value is still higher than that in the infinite array configuration, and is comparable to the depth of the burial.

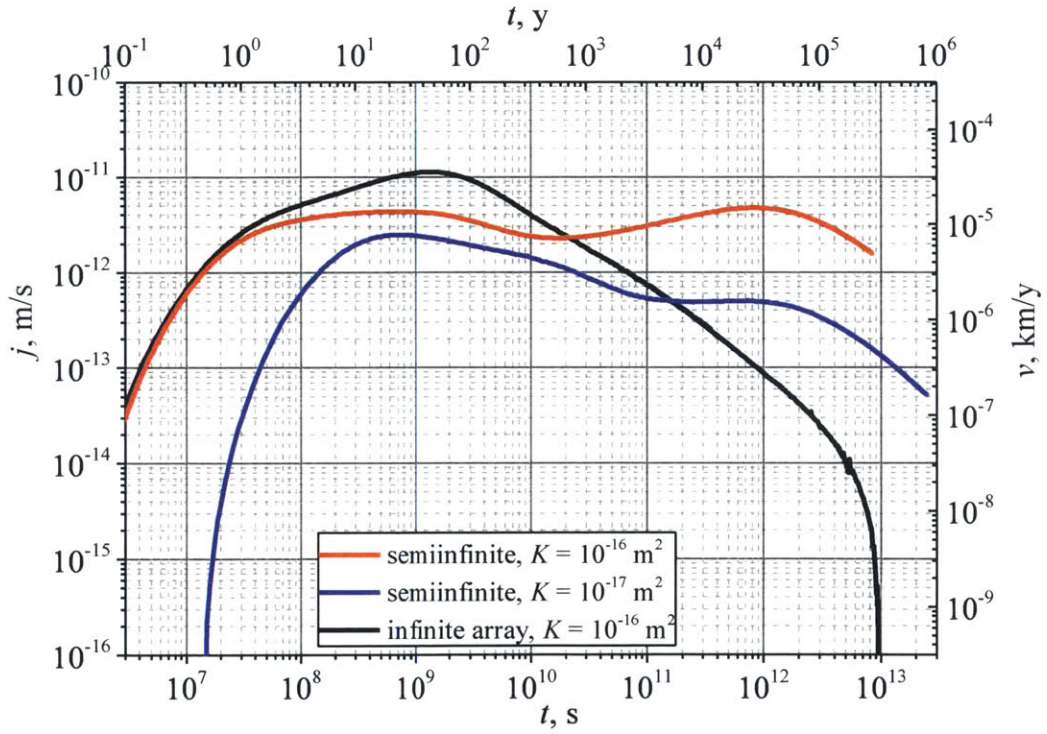

Figure 28. Vertical component of the velocity above the center borehole in the semi-infinite array and above the borehole in the infinite array at the depth of 2 km

The convection rate in the repository is defined by the temperature difference between the repository and the surrounding undisturbed rock. The convection onsets at around 10,000 years since the fuel emplacement, which corresponds to the second peak in temperature. For this reason any measures that reduce the magnitude of the thermal peak should also reduce the convection. This includes reduction in the linear decay power in the boreholes as well as the increase of the pitch length. Reduction of the length of the emplacement zone should also decrease the driving pressure.

6.2.2. Saline Water

The presented results were obtained with the assumption of pure groundwater and no salinity. In reality, the salinity of the water in the rock increases with depth. The highest gradient of salinity is observed at the depth of 1-2 km, and below that depth the salinity remains constant (Eq. (2.36)). It is expected that correct accounting for the salinity gradient could significantly change the convective behavior of the semi-infinite array of boreholes. When the convective flux of water moves the salinity front upwards it permanently creates a pressure difference in the caprock above the repository compared to the undisturbed rock in the direction that suppresses convection.

The salinity model described in Section 2.2.3 was therefore included in the simulations. Unsurprisingly, it was found that convergence for this setup was even more challenging than for the semi-infinite array without salinity. In particular, the time step never exceeded the value of 8×10^{8} s. This did not allow performing simulations up to the 250,000 years that were reached in the semi-infinite case with the rock permeability of 10^{-16} m^2. The test case with rock permeability of 10^{-16} m^2 reached the physical time of 1000 years but did not show any observable difference from the case without salinity and it is therefore of limited significance. Future work could leverage larger computational resources to finalize these runs.

Nevertheless the simulation with rock permeability of 10^{-17} m^2 has been performed up to 70,000 years. The results shown in Figure 29 indicate that the superficial velocity drops by the factor of 4 by the end of the simulation. The perturbation to the salinity profile at this moment at the depth of 1.5 km is shown in Figure 30. The additional pressure gradient due to salinity is around 30 Pa/m. Multiplied by the total length of the salinity gradient region of 1,500 m one can obtain the additional pressure of 45 kPa, which is comparable to the driving pressure of convection.

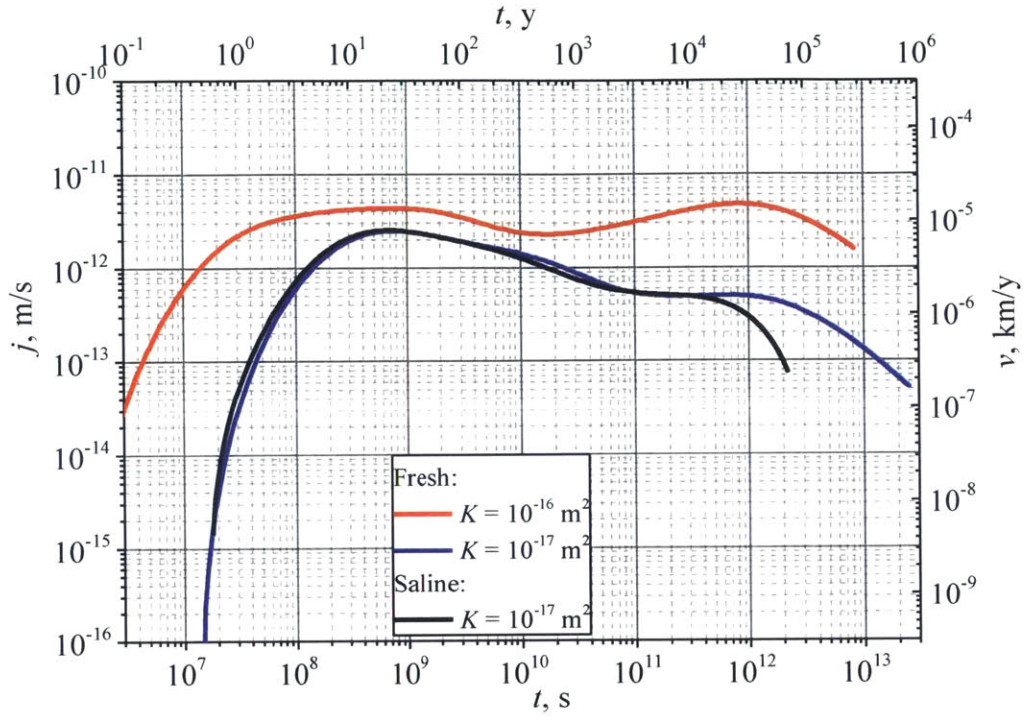

Figure 29. Vertical component of the velocity above the center borehole in the semi-infinite array at the depth of 2 km for fresh and saline water

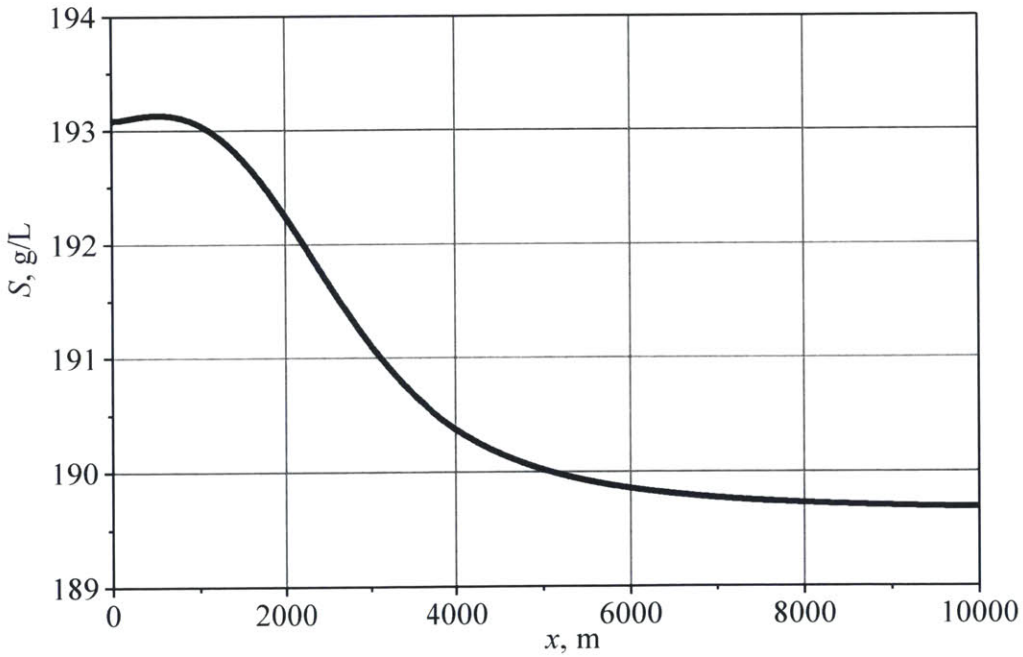

Figure 30. Salinity profile at the depth of 1500 m above the repository 70,000 years after fuel emplacement

7. Summary, Conclusions, and Recommendations

7.1. Summary

Realistic analysis of a deep borehole repository is significant for assessment of its performance and identification of potential weaknesses and failure mechanisms. These analyses should include all significant phenomena, which are physically coupled, with sufficient spatial and temporal resolution of all processes.

In the present work a coupled thermal-hydrological model of the deep borehole repository has been implemented in the FALCON application, leveraging the MOOSE framework. All necessary physical models and correlations were added to the FALCON application and have been presented in this work. A set of computational best practices was identified for optimal numerical performance. The code has been verified on Rayleigh-Bénard convection, and validated using the data for thermal-hydrologic performance of a single borehole, as well as the thermal transient analysis of an infinite array. Valuable results have been obtained and discussed for two representative geometrical configurations of the repository.

7.2. Conclusions

The results of the modeling of the infinite array of boreholes showed that for this configuration the flow in the caprock is dominated by water expansion in both short and long terms. Due to the high aspect ratio of the geometry, superficial velocities were found to be uniform across the horizontal plane. Some water convection has been observed in the emplacement region, however, it decreases in the long term when the temperature profiles become more uniform and it does not contribute to the release of the radionuclides to the ground surface from the repository.

Water flow in the caprock resulted in a maximum upward displacement of water of 30 m, which is the upper theoretical limit of the distance of radionuclide propagation upward from the highest point of the repository. The maximum distance is reached at around 300,000 years after the emplacement, after which the flow reverses due to cooling of the repository. The maximum upward displacement can be higher in the presence of the seal with its higher average permeability, and it was found to be proportional to the ratio of seal to rock permeabilities. This can cause a maximum upward displacement in the seal of 3000 m for a seal permeability of 10 times the rock permeability.

It was shown that in the semi-infinite array configuration the flow is dominated by thermal expansion only during the first thousands of years since the emplacement. A convective cell is formed between the warmer emplacement region and the colder surrounding rock. This resulted in seepage velocities of the order of 10^{-5} km/y over the time span of 200,000 years, and the resulting maximum upward displacements of 2,390 m and 987 m for rock permeabilities of 10^{-16} m^2 and 10^{-17} m^2, respectively. Such maximum upward displacement in the host rock is comparable to the burial depth of the fuel and may cause the release of the radioactive material to the surface.

A possible mechanism that may eliminate convection is the existence of a salinity gradient in natural granitic rocks. The upward displacement of water above the repository is positive while that above the undisturbed rock is negative. The resulting movement of the solute creates an additional pressure, which tend to suppress convection. Even at the time of 70,000 years since the

emplacement the velocity for a test case including salinity was 4 times lower than the velocity in the pure water case.

The results of the modeling of the semi-infinite array led to a number of important conclusions:

1) The infinite array geometry is the most conservative case for the thermal analysis of the performance of the deep boreholes repository, but it imposes unphysical restrictions on the potential flow of the ground water, suppressing the convection between the repository and the undisturbed rock. The infinite array can be adopted for the thermal analysis, but more detailed models should be considered for coupled thermal-hydrologic studies.
2) The modeling shows that in the semi-infinite array configuration the superficial velocity does not drop exponentially over the period of time between 10 years and 100,000 years like in the infinite array. This supports the requirement to model the deep borehole repository for 1,000,000 years since the fuel emplacement.
3) Modeling of the salinity can be important for the performance of the deep borehole repository, as it has been shown to noticeably suppress convection.

This work has also evidenced remaining challenges in the robustness of the adopted numerical methods for many of the analyzed cases. The performance of the Newton solver was found to be superior to the performance of the PJFNK solver, which indicated the need for improved preconditioning to take full advantage of the JFNK approach. However, performance of the Newton solver decreases when the solution becomes advection dominated, and limits the maximum time step at which the code converges. This behavior was observed for both Bénard-Rayleigh convection modeling and the modeling of the semi-infinite array. This restriction did not allow achieving results for the total simulation time of 1,000,000 years.

7.3. Recommendations for Future Work

Recommendations for future work can be divided into code improvements and model improvements.

The code has demonstrated limited robustness when the solution was dominated by the presence of convection, as is the case for the Bénard-Rayleigh convection and a semi-infinite array of boreholes. In both cases, the code could not preserve large time steps, which had to be considerably reduced in order to achieve a converged solution.

Development and testing of improved physics based preconditioning methods have the potential to address this limitation and would further allow adopting effectively the PJFNK solver, which is a key feature of the MOOSE framework.

In the present work the focus has mainly been the support for a conceptual design of a borehole repository. For this reason, a number of simplifications has been made in the derivation of the governing equations and in the description of reference model parameters. More realistic functions for permeability and especially porosity dependence on the depth will instead be required for the accurate evaluation of a realistic borehole design, in particular when evaluating the convective flows close to the bottom boundary in the semi-infinite array configuration.

Two potentially significant phenomena were neglected in this work. First it was assumed that no measurable cracks exist in the rock, and therefore water flow could be described using the isotropic Darcy equation, which averages the flow through a network of small cracks while using an average permeability of the rock. However, local increase in permeability for the seal has shown to have potential to significantly enhance the water velocity. Thick cracks in the host rock may act in the similar way and create a mechanism for the rapid escape of radionuclides. The presence of cracks could be included in future models as highly permeable two-dimensional structures embedded in the three-dimensional uniformly conducting medium.

The second valuable improvement could be the implementation in the code of a mechanical model of the rock. The model could be coupled to the thermal model through expansion coefficients of the rock, and to the hydrologic model via permeability and porosity. Implementation of the mechanical properties would complete the coupled thermal-hydrologic-mechanical-chemical formulation and allow simulating all the processes that are expected to be significant in a borehole repository.

References

[1] E. A. Bates, "A Drop-In Concept for Deep Borehole Canister Emplacement," Master of Science Thesis, Massachusetts Institute of Technology, 2011.

[2] J. Wagner, J. Peterson, D. Mueller, J. Gehin, A. Worall, T. Taiwo, M. Nutt, M. Williamson, M. Todosow, W. Halsey, R. Omberg, P. Swift and J. Carter, "Categorization of Used Nuclear Fuel Inventory in Support of a Comprehensive National Nuclear Fuel Cycle Strategy," Oak Ridge National Laboratory, Oak Ridge, TN, ORNL/TM-2012/308, 2012.

[3] Woodward-Clyde Consultants, "Very Deep Hole Systems Engineering Studies," prepared for Office of Nuclear Waste Isolation, Battelle Memorial Institute, Columbus, OH, ONWI-226, December 1983.

[4] J. Bodenes, L. Dewiere, P. Oustriere, J. Aussier, A. Menjoz, J. Sauty and M. Vauclin, "Modelling Heat Transfer Near a Deep Underground Nuclear Waste Repository: a Discussion of Boundary Conditions," in *Proceedings of ModelCARE 90: Calibration and Reliability in Groundwater Modelling*, The Hague, 1990.

[5] E. A. Bates, J. Buongiorno, E. Baglietto and M. J. Driscoll, "Transient Thermal Modeling of a Deep Borehole Repository," in *Transactions of the American Nuclear Society, Vol. 106*, Chicago, IL, 2012.

[6] J. Claesson, "Buoyancy Flow in Fractured Rock with a Salt Gradient in the Groundwater – An Initial Study," Department of Building Physics, Lund University, Sweden, SKB TR 92-05, Feb. 1992.

[7] J. Claesson, G. Hellström and T. Probert, "Buoyancy Flow in Fractured Rock with a Salt Gradient in the Groundwater. A Second Study of Coupled Salt and Thermal Buoyancy," Depts. of Building Physics and Mathematical Physics, Lund University, Sweden, SKB TR 92-41, Nov. 1992.

[8] G. A. Zyvolosky, B. A. Robinson, Z. V. Dash and L. L. Trease, "Summary of the Models and Methods for the FEHM Application - A Finite-Element Heat- and Mass-Transfer Code," Los Alamos National Laboratory, LA-13307-MS, 1997.

[9] B. Arnold, T. Hadgu, D. Clayton and C. Herrick, "Thermal-hydrologic-chemical-mechanical Modeling of Deep Borehole Disposal," in *Proceedings of the 13th International High-level Radioactive Waste Management Conference*, Albuquerque, NM, 2011.

[10] R. Podgorney, H. Huang and D. Gaston, "Massively Parallel Fully Coupled Implicit Modeling of Coupled Thermal-hydrological-mechanical Processes for Enhanced Geothermal System Reservoirs," in *Thirty-Fifth Workshop on Geothermal Reservoir Engineering*, Stanford, CA, Feb. 2010.

[11] D. Gaston, C. Newman, G. Hansen and D. Lebrun-Grandié, "MOOSE: A Parallel Computational Framework for Coupled Systems of Nonlinear Equations," *Nuclear Engineering and Design,* vol. 239, pp. 1768-1778, 2009.

[12] "MOOSE Workshop Training Manual," 2014. [Online]. Available: http://mooseframework.com/static/media/uploads/docs/main.pdf.

[13] R. A. Knief, Nuclear Engineering: Theory and Technology of Commercial Nuclear Power, La Grange Park, IL: American Nuclear Society, 2008.

[14] S. Ingebritsen, W. Sanford and C. Neuzil, Groundwater in Geologic Processes, Cambridge, UK: Cambridge University Press, 2006.

[15] M. Gascoyne, "Hydrogeochemistry, Groundwater Ages and Sources of Salts in a Granitic Batholith on the Canadian Shield, Southeastern Manitoba," *Applied Geochemistry,* vol. 19, no. 4, pp. 519-560, 2004.

[16] J. T. Carter, A. J. Luptak, J. Gastelum, C. Stockman and A. Miller, "Fuel Cycle Potential Waste Inventory for Disposition," U.S. Department of Energy, FCR&D-USED-2010-000031 Rev 5, 2012.

[17] American Nuclear Society, "American National Standard "Decay Heat Power in Light Water Reactors"," American Nuclear Society, La Grange Park, IL, 2014.

[18] C. I. Hoag, "Canister Design for Deep Borehole Disposal of Nuclear Waste," Master of Science Thesis, Massachusetts Institute of Technology, 2005.

[19] J. Bear, Hydraulics of Groundwater, New York, NY: McGraw-Hill, Inc., 2007.

[20] J. Townend and M. Zoback, "How Faulting Keeps the Crust Strong," *Geology,* vol. 28, pp. 399-402, 2000.

[21] E. A. Bates, "Optimization of Deep Boreholes for Disposal of High-Level Nuclear Waste," Doctoral Thesis, Massachusetts Institute of Technology, 2015.

[22] W. DeMaio and E. Bates, "Salinity and Density in Deep Boreholes," *Massachusetts Institute of Technology Undergraduate Research Journal,* vol. 26, pp. 42-48, 2013.

[23] B. W. Arnold and T. Hadgu, "Thermal-Hydrologic Modeling of a Deep Borehole Disposal System," in *Proceedings of the 14th International High-level Radioactive Waste Management Conference*, Albuquerque, NM, 2013.

[24] P. Vilks, J. Cramer, M. Jensen, N. Miller, H. Miller and F. Stanchell, "In Situ Diffusion Experiment in Granite: Phase I," *Journal of Contaminant Hydrology,* vol. 61, pp. 191-202, 2003.

[25] C. Manning and S. Ingebritsen, "Permeability of the Continental Crust: Implications of Geothermal Data and Metamorphic Systems," *Reviews of Geophysics,* vol. 37, p. 127–150, 1999.

[26] C. Juhlin and H. Sandstedt, "Storage of Nuclear Waste in Very Deep Boreholes: Feasibility Study and Assessment of Economic Potential," SKB, Stockholm, Sweden, SKB TR 89-39, Dec. 1989.

[27] F. G. F. Gibb, K. P. Travis, N. A. McTaggart and D. Burley, "A Model for Heat Flow in Deep Borehole Disposals of High-level Nuclear Waste," *Journal of Geophysical Research,* vol. 113, 2008.

[28] B. W. Arnold, P. V. Brady, S. J. Bauer, C. Herrick, S. Pye and J. Finger, "Reference Design and Operations for Deep Borehole Disposal of High-Level Radioactive Waste," Sandia National Laboratories, Albuquerque, NM, SAND2011-6749, 2011.

[29] W.-S. Kuo, "Evaluation of Deep Drillholes for High Level Nuclear Waste Disposal," Master of Science Thesis, Massachusetts Institute of Technology, 1991.

[30] C. Malbrain, R. Lester and J. Deutch, "Analytical Approximations for the Long Term Decay Behavior of Spent Fuel and High Level Waste," *Nuclear Technology,* vol. 57, p. 292, 1982.

[31] R. Podgorney, H. Huang, C. Lu, D. Gaston, C. Permann, L. Guo and D. Andrs, "FALCON: a Physics-based, Massively Parallel, Fully-coupled, Finite Element Model for Simultaneously Solving Multiphase Fluid Flow, Heat Transport, and Rock Deformation for Geothermal Reservoir Simulation," Idaho National Laboratory, Idaho Falls, ID, Report INL/EXT-11-23351, 2011.

[32] F. Milliero, C.-T. Chen, A. Bradshaw and K. Schleicher, "A New High Pressure Equation of State for Seawater," *Deep Sea Research Part A. Oceanographic Research Papers,* vol. 27, no. 3-4, pp. 255-264, 1980.

[33] B. S. Kirk, J. Peterson, R. H. Stogner and G. F. Carey, "libMesh: a C++ Library for Parallel Adaptive Mesh Refinement/Coarsening Simulations," *Engineering with Computers,* Vols. 22(3-4), p. 237–254, Jan. 2006.

[34] S. Balay, K. Buschelman, V. Eijkhout, W. D. Gropp, D. Kaushik, M. G. Knepley, L. C. McInnes, B. F. Smith and H. Zhang, "PETSc Users Manual," Argonne National Laboratory, Technical Report ANL-95/11 - Revision 2.1.5, 2004.

[35] D. A. Knoll and D. E. Keyes, "Jacobian-free Newton-Krylov Methods: a Survey of Approaches and Applications," *Journal of Computational Physics,* vol. 193, no. 2, p. 357–397, 2004.

[36] T. J. Hughes and M. Mallet, " A New Finite Element Formulation for Computational Fluid Dynamics: III. The Generalized Streamline Operator for Multidimensional Advective-diffusive Systems," *Computer Methods in Applied Mechanics and Engineering,* vol. 58, no. 3, pp. 305-328, 1986.

[37] "CUBIT 13.2 User Documentation," Sandia National Laboratories, Albuquerque, NM, 2012.

[38] D. Gaston, *personal communication,* MIT, 2014.

[39] K.-K. Tan, T. Sam and H. Jamaludin, "The Onset of Transient Convection in Bottom Heated Porous Media," *International Journal of Heat and Mass Transfer,* vol. 46, pp. 2857-2873, 2003.

Appendix A. Average Heat Generation Table for PWR Fuel

This table summarizes the decay heat correlation used in [23]. The data were kindly provided by Bill Arnold.

Table 10. Decay heat power for cross-code validation.

t, y	Total power per borehole q, kW	Volumetric power in homogenized boreholes q''', W/m^3
0	430.56	2371.1
1	430.56	2371.1
2	426.23	2347.3
3	421.96	2323.8
4	417.75	2300.6
5	413.59	2277.7
6	409.48	2255.0
7	405.42	2232.7
8	401.41	2210.6
9	397.45	2188.8
10	393.54	2167.3
20	357.02	1966.1
30	324.80	1788.7
40	296.35	1632.0
50	271.22	1493.6
60	249.02	1371.4
70	229.39	1263.3
80	212.03	1167.7
90	196.67	1083.1
100	183.06	1008.1
125	155.40	855.78
150	134.81	742.42
175	119.38	657.44
200	107.70	593.14
225	98.770	543.94
250	91.840	505.77
275	86.378	475.69
300	81.997	451.56
325	78.411	431.82
350	75.417	415.33
375	72.865	401.27
400	70.645	389.05
425	68.677	378.21
450	66.904	368.45
475	65.284	359.52
500	63.784	351.27
550	61.061	336.27

600	58.614	322.79
650	56.374	310.46
700	54.301	299.04
750	52.371	288.41
800	50.566	278.47
850	48.874	269.16
900	47.287	260.42
950	45.796	252.21
1000	44.395	244.49
1100	41.837	230.40
1200	39.571	217.92
1300	37.559	206.84
1400	35.770	196.99
1500	34.176	188.21
1600	32.753	180.37
1700	31.479	173.36
1800	30.337	167.07
1900	29.309	161.41
2000	28.382	156.30
2100	27.543	151.68
2200	26.781	147.49
2300	26.088	143.67
2400	25.455	140.18
2500	24.874	136.98
2600	24.340	134.04
2700	23.846	131.32
2800	23.388	128.80
2900	22.963	126.46
3000	22.565	124.27
3100	22.193	122.22
3200	21.842	120.29
3300	21.511	118.46
3400	21.197	116.74
3500	20.900	115.10
3600	20.616	113.53
3700	20.344	112.04
3800	20.084	110.60
3900	19.833	109.22
4000	19.592	107.90
4100	19.359	106.61
4200	19.134	105.37
4300	18.915	104.17
4400	18.703	103.00
4500	18.496	101.86
4600	18.295	100.75
4700	18.099	99.670

4800	17.907	98.613
4900	17.719	97.580
5000	17.535	96.568
5200	17.179	94.604
5400	16.835	92.713
5600	16.504	90.887
5800	16.183	89.121
6000	15.872	87.410
6200	15.571	85.751
6400	15.278	84.139
6600	14.994	82.573
6800	14.717	81.050
7000	14.448	79.568
7200	14.186	78.126
7400	13.931	76.721
7600	13.683	75.354
7800	13.441	74.021
8000	13.205	72.723
8200	12.975	71.457
8400	12.751	70.224
8600	12.533	69.021
8800	12.320	67.849
9000	12.113	66.706
9200	11.910	65.591
9400	11.713	64.504
9600	11.520	63.444
9800	11.333	62.409
10000	11.149	61.400
11000	10.298	56.712
12000	9.5443	52.562
13000	8.8756	48.879
14000	8.2809	45.604
15000	7.7510	42.685
16000	7.2775	40.078
17000	6.8535	37.743
18000	6.4726	35.645
19000	6.1296	33.756
20000	5.8197	32.050
21000	5.5389	30.503
22000	5.2837	29.098
23000	5.0509	27.816
24000	4.8380	26.643
25000	4.6426	25.567
26000	4.4626	24.576
27000	4.2963	23.660
28000	4.1422	22.811

29000	3.9988	22.022
30000	3.8652	21.286
31000	3.7401	20.597
32000	3.6227	19.951
33000	3.5123	19.342
34000	3.4081	18.769
35000	3.3096	18.226
36000	3.2161	17.711
37000	3.1273	17.223
38000	3.0428	16.757
39000	2.9622	16.313
40000	2.8851	15.888
41000	2.8113	15.482
42000	2.7405	15.092
43000	2.6726	14.718
44000	2.6072	14.358
45000	2.5443	14.012
46000	2.4837	13.678
47000	2.4253	13.356
48000	2.3688	13.045
49000	2.3143	12.745
50000	2.2616	12.455
51000	2.2105	12.174
52000	2.1611	11.902
53000	2.1133	11.638
54000	2.0669	11.383
55000	2.0219	11.135
56000	1.9783	10.895
57000	1.9360	10.662
58000	1.8949	10.435
59000	1.8550	10.216
60000	1.8163	10.002
61000	1.7786	9.7952
62000	1.7421	9.5938
63000	1.7066	9.3981
64000	1.6720	9.2080
65000	1.6384	9.0231
66000	1.6058	8.8433
67000	1.5741	8.6685
68000	1.5432	8.4986
69000	1.5132	8.3333
70000	1.4840	8.1725
71000	1.4556	8.0161
72000	1.4280	7.8639
73000	1.4011	7.7159
74000	1.3749	7.5719

75000	1.3495	7.4317
76000	1.3247	7.2953
77000	1.3006	7.1626
78000	1.2772	7.0335
79000	1.2543	6.9078
80000	1.2321	6.7855
81000	1.2105	6.6664
82000	1.1895	6.5506
83000	1.1690	6.4378
84000	1.1491	6.3280
85000	1.1296	6.2211
86000	1.1108	6.1170
87000	1.0924	6.0158
88000	1.0745	5.9172
89000	1.0570	5.8212
90000	1.0401	5.7277
91000	1.0235	5.6367
92000	1.0074	5.5481
93000	0.99179	5.4619
94000	0.97653	5.3779
95000	0.96168	5.2961
96000	0.94722	5.2164
97000	0.93314	5.1389
98000	0.91943	5.0634
99000	0.90607	4.9898
100000	0.89307	4.9182
110000	0.78025	4.2969
120000	0.69338	3.8185
130000	0.62621	3.4486
140000	0.57401	3.1612
150000	0.53321	2.9364
160000	0.50106	2.7594
170000	0.47549	2.6186
180000	0.45495	2.5054
190000	0.43822	2.4133
200000	0.42441	2.3373
210000	0.41282	2.2735
220000	0.40294	2.2190
230000	0.39437	2.1718
240000	0.38680	2.1301
250000	0.38000	2.0927
260000	0.37381	2.0586
270000	0.36809	2.0271
280000	0.36273	1.9976
290000	0.35767	1.9697
300000	0.35284	1.9431

310000	0.34820	1.9176
320000	0.34371	1.8929
330000	0.33936	1.8689
340000	0.33511	1.8455
350000	0.33096	1.8226
360000	0.32689	1.8002
370000	0.32289	1.7782
380000	0.31896	1.7566
390000	0.31510	1.7353
400000	0.31129	1.7143
410000	0.30753	1.6936
420000	0.30383	1.6732
430000	0.30017	1.6531
440000	0.29656	1.6332
450000	0.29300	1.6136
460000	0.28948	1.5942
470000	0.28601	1.5751
480000	0.28258	1.5562
490000	0.27919	1.5375
500000	0.27585	1.5191
510000	0.27254	1.5009
520000	0.26927	1.4829
530000	0.26605	1.4651
540000	0.26286	1.4476
550000	0.25971	1.4302
560000	0.25660	1.4131
570000	0.25352	1.3962
580000	0.25048	1.3794
590000	0.24748	1.3629
600000	0.24452	1.3466
610000	0.24159	1.3305
620000	0.23869	1.3145
630000	0.23583	1.2988
640000	0.23301	1.2832
650000	0.23022	1.2678
660000	0.22746	1.2526
670000	0.22473	1.2376
680000	0.22204	1.2228
690000	0.21938	1.2082
700000	0.21675	1.1937
710000	0.21416	1.1794
720000	0.21159	1.1652
730000	0.20906	1.1513
740000	0.20655	1.1375
750000	0.20408	1.1239
760000	0.20163	1.1104

770000	0.19922	1.0971
780000	0.19683	1.0840
790000	0.19447	1.0710
800000	0.19214	1.0581
810000	0.18984	1.0455
820000	0.18756	1.0329
830000	0.18532	1.0206
840000	0.18310	1.0083
850000	0.18090	0.99625
860000	0.17874	0.98432
870000	0.17660	0.97253
880000	0.17448	0.96088
890000	0.17239	0.94936
900000	0.17032	0.93799
910000	0.16828	0.92675
920000	0.16627	0.91565
930000	0.16428	0.90468
940000	0.16231	0.89384
950000	0.16036	0.88313
960000	0.15844	0.87255
970000	0.15654	0.86210
980000	0.15467	0.85177
990000	0.15281	0.84157
1000000	0.15098	0.83148